Optimization of interneuron function by direct coupling of cell migration and axonal targeting

Lynette Lim[1,2,3], **Janelle MP Pakan**[#4], **Martijn M Selten**[#1,2], **André Marques-Smith**[1,2], **Alfredo Llorca**[1,2], **Sung Eun Bae**[1,2], **Nathalie L Rochefort**[4,5], and **Oscar Marín**[1,2,3]

[1]Centre for Developmental Neurobiology, Institute of Psychiatry, Psychology and Neuroscience, King's College London, London SE1 1UL, United Kingdom

[2]MRC Centre for Neurodevelopmental Disorders, King's College London, London SE1 1UL, United Kingdom

[3]Instituto de Neurociencias, Consejo Superior de Investigaciones Científicas & Universidad Miguel Hernández, Sant Joan d'Alacant 03550, Spain

[4]Centre for Integrative Physiology, School of Biomedical Sciences, University of Edinburgh, Edinburgh, United Kingdom

[5]Simons Initiative for the Developing Brain, University of Edinburgh, Edinburgh, EH8 9XD UK

[#] These authors contributed equally to this work.

Abstract

Neural circuit assembly relies on the precise synchronization of developmental processes such as cell migration and axon targeting, but the cell autonomous mechanisms coordinating these events remain largely unknown. Here we found that different classes of interneurons use distinct routes of migration to reach the embryonic cerebral cortex. Somatostatin-expressing interneurons that migrate through the marginal zone develop into Martinotti cells, one of the most distinctive class of cortical interneurons. For these cells, migration through the marginal zone is linked to the development of their characteristic layer 1 axonal arborization. Alteration of the normal migratory route of Martinotti cells by conditional deletion of *Mafb* – a gene that is preferentially expressed by these cells – cell-autonomously disrupts axonal development and impairs the function of these

cells in vivo. Our results suggest that migration and axon targeting programs are coupled to optimize the assembly of inhibitory circuits in the cerebral cortex.

The assembly of neural circuits involves a series of highly coordinated events, from cell fate specification and neuronal migration to the precise targeting of synaptic connections. While these processes are often studied separately, they must have been efficiently linked during evolution to optimize the formation of neural circuits. For instance, migrating pioneer neurons establish permissive environments for specific brain connections[1–4], whereas the allocation of neurons into segregated cell layers facilitates the rapid assembly of functional networks[5]. However, links between cell fate specification, neuronal migration and precise axonal targeting remain largely unexplored.

Neural circuits in the cerebral cortex consist of two major classes of neuron, excitatory pyramidal cells and inhibitory GABAergic interneurons. Cortical interneurons are highly heterogeneous, comprising several functional classes with unique morphological, electrophysiological and molecular features[6]. Recent transcriptomic analyses in the mouse adult neocortex have identified over 20 molecularly distinct classes of interneurons[7,8]. Although different classes of interneurons cannot be distinguished based on a unique criterion[9], axonal arborization is a major classification feature since it largely determines the function of interneurons in neural circuits[6,10].

Cortical interneurons can also be classified based on their developmental origin and expression of key molecular markers[6]. Most interneurons derive from the medial ganglionic eminence (MGE) and belong to two major groups, Parvalbumin-expressing (PV+) and Somatostatin-expressing (SST+) interneurons[11]. This later group encompasses at least two major classes of cells, which can be distinguished by the presence (Martinotti cells) or absence of a dense axonal plexus in layer 1[12–15]. The remaining classes of cortical interneurons originate in the caudal ganglionic eminence (CGE) and in the preoptic area (POA)[16].

Interneurons reach the embryonic cortex via two highly stereotyped routes, the marginal zone (MZ) and the subventricular zone (SVZ)[17], but the logic behind the segregation of interneurons into different migratory streams remains unclear. One possibility is that interneurons are specified into distinct classes before reaching the cortex and the selection of a particular migratory route is part of an unfolding program of neuronal differentiation. This hypothesis is supported by inter-species transplantation experiments, which showed that the ability of interneurons to use distinct migratory routes differs between species[18]. Alternatively, interneuron specification might be influenced by the local environment in the cortex[19], and so migratory route allocation might be independent of interneuron specification.

Here we found that different types of embryonic SST+ interneurons use distinct routes of migration through the embryonic cortex. In particular, Martinotti cells display a strong preference for migration through the MZ, a behavior that seems to be linked to the development of their prominent axonal arbor in layer 1. Translaminar PV+ interneurons also migrate preferentially through the MZ, which suggest that this might be a general

mechanism for interneurons with axon arbors spanning across multiple cortical layers. These results suggest that interneurons are committed to distinct cell fates prior to their arrival in the cortex and reveal an unexpected degree of cell-autonomous coordination between different developmental programs during the assembly of neural circuits.

Results

Migratory route choice varies among different classes of interneurons

We investigated whether migratory route preference (SVZ vs. MZ) varies during embryonic development using *Vgat^Cre;RCE* mice, in which all GABAergic interneurons are labeled with GFP. Most interneurons (~75%) migrate via the SVZ and this preference remains relatively constant during development (Fig. 1a–d). We asked whether interneurons originating in different regions of the subpallium – MGE, CGE or POA – have distinct migratory route preferences. We quantified the SVZ/MZ ratio for interneurons derived from the MGE/POA and CGE using *Nkx2-1-Cre;RCE* and *Gad65-GFP* mice, respectively. The fraction of MGE/POA- and CGE-derived interneurons migrating through the MZ is very similar (~25%), and remains constant at different stages (Fig. 1e–g,j). These observations confirmed that migratory route choice is not determined by the place of origin of interneurons[20].

We next wondered whether specific classes of interneurons prefer different migratory routes. Because SST is the only neurochemical marker that is expressed by migrating interneurons embryonically, we analyzed the SVZ/MZ ratio for SST+ interneurons using *Sst^Cre;Ai9* mice. We found a much higher proportion of SST+ interneurons migrating through the MZ (~50%) than expected from the analysis of *Nkx2-1-Cre;RCE* mice (Fig. 1g,h,j). Similar results were obtained using *Dlx1/2^CreER* mice (Fig. 1g,i,j), a "leaky" transgenic strain that labels sparse SST+ interneurons (along with some prospective PV+ interneurons) when crossed with a reporter line in the absence of tamoxifen (Supplementary Fig. 1)[21]. These results suggested that cortical interneurons are not randomly allocated to any migratory route.

Migratory route choice is stable and cell-autonomous

We reasoned that if the fate of a specific class of interneurons is linked to a migratory route, then interneurons should remain in the same migratory route once they have made a choice. To test this idea, we electroporated the MGE of embryonic day (E) 13.5 *Nkx2-1-Cre* mouse embryos with a plasmid conditionally encoding Kikume Green-Red, a photoconvertible green-to-red fluorescent protein[22]. Forty-eight hours later, we photoconverted individual interneurons in the MZ and tracked their migratory behavior for 14 hours (Supplementary Fig. 2a and Supplementary Video 1). Most interneurons migrating through the MZ remain within this route during this period (Supplementary Fig. 2b,c,e), even though many should have abandoned this route during that time based on their normal migratory speed (Supplementary Fig. 2d,e).

We devised a transplantation experiment to test whether migrating interneurons are cell-autonomously committed to a particular migratory route (Supplementary Fig. 2f). We

obtained cell suspensions by physically separating the MZ and the SVZ in E16.5 embryos. In control experiments, we verified the efficiency of this protocol in *Calb2^Cre^;Ai9* embryos, in which the first fraction obtained was enriched in Cajal-Retzius cells (tdTomato+), while fractions fourth and fifth were enriched in SVZ Tbr2+ cells (Supplementary Fig. 3). We transplanted MZ or SVZ cells from *Nkx2-1-Cre;Ai9* embryos into the pallial/subpallial boundary of acute slices obtained from wild type embryos (Supplementary Fig. 2f). We found that migrating interneurons have a strong inclination to use the same route from which they were isolated (Supplementary Fig. 2g–i), which reinforced the idea that interneurons are committed to a particular route of migration.

SST+ interneurons in the MZ and SVZ unfold distinct molecular programs

Migrating interneurons have identical morphology regardless of their origin or migratory route[23,24]. To investigate whether SST+ cells migrating through different routes are molecularly distinct, we carried out RNAseq analyses using SST+ cells isolated from the MZ and SVZ using the method described above (Supplementary Fig. 3). We found 81 genes to be differentially expressed (DEseq R analysis, FDR < 5%) between both populations of cells, of which 24 genes are upregulated in SST+ interneurons migrating through the MZ compared to the SVZ (Fig. 2a,d and Supplementary Fig. 4).

We wondered whether the genes enriched in either MZ or SVZ SST+ cells correspond to genes that are differentially expressed by distinct classes of interneurons in the adult cortex. To answer this question, we took advantage of recent single cell RNAseq studies that unbiasedly identified six different groups of SST+ cells in the visual cortex of adult mice[8]. We assessed mean z-scores for the 81 differentially expressed genes in different groups of adult SST+ interneurons (Fig. 2b and Supplementary Fig. 5). We found that genes enriched in SST+ interneurons migrating through the embryonic MZ have mean positive z-scores that mostly clustered within three main subtypes of SST+ interneurons, *Cdk6+*, *Cbln4+*, and *Myh8+* cells (Fig. 2b,c). In contrast, these genes have negative z-scores for SST+ interneurons characterized by the expression of *Chodl* (Fig. 2b,c). Conversely, genes enriched in SST+ cells migrating through the embryonic SVZ have mean positive z-scores in *Chodl+* interneurons, but negative scores in all the other five groups of SST+ interneurons (Fig. 2c and Supplementary Fig. 5a,b). These results strongly suggested that SST+ interneurons migrating through the embryonic MZ and SVZ of the developing cortex correspond to different populations of SST+ interneurons in the adult cortex.

We also assessed mean z-scores for individual genes enriched in the MZ, and found that only 3 out of 24 genes are positively enriched in one population of SST+ interneurons, and selectively de-enriched in the other five populations (Fig. 2e). Specifically, *Mafb*, *Maf* and *Chl1* were found to be particularly enriched in *Cbln4+* population, a gene enriched in Martinotti cells[8]. In addition, we also observed that *Chrna2*, a specific marker of layer 5 Martinotti cells[25], is highly enriched in both *Cdk6+* and *Myh8+* cell populations (Supplementary Fig. 5c). This analysis prompted us to test whether SST+ migrating through the embryonic MZ are prospective Martinotti cells.

Martinotti cells preferentially migrate through the MZ

Electrophysiological and morphological studies have shown that SST+ interneurons comprise at least two functionally distinct classes of interneurons: (i) layer 1-targeting Martinotti cells, and (ii) locally-projecting SST+ interneurons[12,13,15]. Unbiased labeling of interneuron progenitor cells at E14.5 in *Sst*[Cre] embryos (Fig. 3a) revealed that 60% of SST+ interneurons populating layer 2/3 have large axonal arbors in layer 1, a characteristic feature of Martinotti cells (Fig. 3b,e), while the remaining are locally projecting SST+ interneurons (Fig. 3e,f). To test if prospective Martinotti cells preferentially migrate through the MZ, we carried out pial surface electroporation experiments (Supplementary Fig. 6)[26] using a conditional reporter plasmid to specifically target SST+ cells in this stream (Fig. 3c). To compare these results with the retroviral labeling experiments, we targeted the cortex of *Sst*[Cre] pups immediately after birth, when a large fraction of layer 2/3 MGE-derived interneurons is still migrating tangentially[27]. As predicted from our bioinformatic analyses, we found that the vast majority of SST+ cells migrating through the MZ at this stage give rise to interneurons with the morphology of Martinotti cells (90%; Fig. 3d,g,e). We also observed a substantial number of labeled SST+ interneurons in layer 5, the majority having the morphology of Martinotti cells (87%; Supplementary Fig. 7). In contrast, the fraction of labeled SST+ cells found in layer 4, which mostly contains locally projecting SST+ interneurons[15], was very small (Supplementary Fig. 7). These experiments indicated that SST+ cells migrating through the MZ become Martinotti cells.

Translaminar PV+ interneurons also migrate through the MZ

We next wondered whether other interneurons with translaminar axons similar to Martinotti cells would also preferentially migrate through the MZ. Although most PV+ interneurons are basket cells whose axons arborize in the same layer where the cell soma is located[6], recent studies have described a small population of deep layer PV+ interneurons with ascending translaminar axons[28,29]. Consistently, unbiased labeling of interneuron progenitor cells at E12.5 in *Pvalb*[Cre] embryos revealed that about 10% of PV+ cells populating layers 5 and 6 are translaminar (Fig. 3h,i,l). By contrast, pial surface electroporation in neonatal *Pvalb*[Cre] pups revealed a much higher proportion of deep layer translaminar PV+ cells (>50%; Fig. 3j,k,l). Similar to Martinotti cells, deep layer translaminar PV+ interneurons preferentially migrate through the MZ.

Martinotti cells leave their nascent axon in the MZ when they enter the cortex

The previous results suggested that interneurons with translaminar axons use the MZ as their migratory route. We hypothesized that this might be directly linked to their axonal morphology, and focused our attention again on Martinotti cells to test this idea. Since the developing MZ becomes layer 1 in the adult cortex and Martinotti cells have an axon in layer 1, we hypothesized that the migration of these cells through the MZ may influence their axonal arborization. To test this hypothesis, we performed time-lapse imaging experiments in slice cultures. Using *Dlx1/2*[CreER];*Ai9* to sparsely label a small population of SST+ cells (Supplementary Fig. 1), we monitored the migration of prospective Martinotti cells at early postnatal stages as they 'dive' into the cortical plate. We observed that most (11 out of 13) SST+ cells that enter the cortical plate from the MZ leave behind a trailing

process (Fig. 4a and Supplementary Video 2), whereas most presumptive PV+ basket cells (Supplementary Fig. 1) using the same migratory stream do not (1 out of 8; Fig. 4c and Supplementary Video 3). We measured the speed of the trailing process in both sets of experiments, and found that only the trailing process of the prospective Martinotti cells remains stationary (Fig. 4b). Moreover, the final distance between the trailing process and the cell soma was significantly larger in SST+ than in presumptive PV+ basket cells (Fig. 4d). Finally, to determine the molecular composition of the trailing process in SST+ cells, we performed pial surface electroporation with a conditional plasmid encoding membrane tdTomato and a truncated form of Kinesin family member 5 (Kif5C 560) that nascent axons30 (Fig. 4e). We found that Kif5C 560 labels the tip of the processes that remain in the MZ (11 out of 14 cells, with 4 non-polarized; Fig. 4f). This finding confirmed that the process left in the MZ by Martinotti cells is the nascent axon.

Abnormal route choices in conditional *Mafb* mutants

We next screened for migration defects in mouse mutants carrying loss of function alleles for some of the genes preferentially expressed by MZ-migrating SST+ interneurons (Fig. 2d). We observed no major changes in the fraction of SST+ cells taking the MZ or SVZ migratory routes in *Neto1* and *Elfn1* mutant mice (Supplementary Fig. 8). In contrast, conditional deletion of *Mafb* from SST+ interneurons led to a small decrease (~20%) in the fraction of SST+ interneurons migrating through the MZ compared to control mice, along with a corresponding increase in SST+ cells in the SVZ (Fig. 5a–d). Despite these changes in route choice, the laminar distribution of SST+ cells in the neocortex of P21 conditional *Mafb* mutants and control is comparable (Fig. 5e–g). Altogether, these experiments suggested that postmitotic MafB expression is required for migratory route allocation by a fraction of prospective Martinotti cells.

Layer 1 axon defects in Martinotti cells from conditional *Mafb* mutants

Although the final number of SST+ interneurons in the neocortex of conditional *Mafb* mutants is normal, our previous analysis showed that a fraction of these interneurons reaches the cortex through an abnormal route. To test whether this may impact the development of axonal arbors by Martinotti cells, we analyzed the density of layer 1 axons (labeled with GFP from the *RCE* allele) in P21 control and conditional *Mafb* mutant mice. We observed a prominent reduction in GFP intensity in layer 1 axons of conditional *Mafb* mutants compared to controls (Fig. 5h–k). To test whether individual axonal arbor of Martinotti cells is affected, we sparsely labeled layer 2/3 Martinotti cells using retrovirus at E14.5 (Fig. 6a). Analysis of these experiments at P21 revealed a fraction of Martinotti cells with poorly developed layer 1 axon in conditional *Mafb* mutant mice (Fig. 6b,c,g). Of note, Martinotti cell axons spanning other cortical layers were comparable between both genotypes, which suggested that the axon arborization phenotype observed in conditional *Mafb* mutants is specific to layer 1 (Fig. 6b,c,h). Moreover, analysis of the axon arbors of non-Martinotti SST + cells revealed no significant differences between controls and conditional *Mafb* mutant mice (Supplementary Fig. 9).

There are three alternative explanations for the observed phenotypes: (1) Loss of MafB changes the fate of Martinotti and these cells do not migrate through the MZ; (2) loss of

MafB disrupts both migration and layer 1 axonal arborization independently; and (3) layer 1 axonal arborization are secondary to the migration phenotypes caused by the loss of MafB. We use the co-expression of Calretinin (CR)31 and Calbindin (CB) (Supplementary Fig. 5c) to molecularly identify prospective Martinotti cells and found comparable fractions of SST +/CR+ and SST+/CB+ interneurons in conditional *Mafb* mutants and controls (Supplementary Fig. 10). To reinforce these results, we performed whole-cell patch clamp recordings from layer 2/3 SST+ cells in the somatosensory cortex. Analysis of SST+ cells with an ascending axonal projection into layer 1, identified by biocytin labeling in patched cells, revealed no significant differences in the intrinsic properties and excitability of Martinotti cells in controls and conditional mutants (Supplementary Fig. 11a–g). Together, these results suggested that loss of *Mafb* does not impact the specification of Martinotti cells.

To distinguish between the other two possibilities, we carried out a new series of experiments. Since a fraction of SST+ cells that migrate normally through the MZ in conditional *Mafb* mutant mice (Fig. 5a–d), these cells should exhibit normal layer 1 axonal morphologies if the defects observed in many Martinotti cells were secondary to defective migration through the MZ. To test this, we performed pial surface electroporation experiments in control and conditional *Mafb* mutant (Fig. 6d). We found that Martinotti cells that have migrated through the MZ develop similar layer 1 axonal arborization in both control and *Mafb* mutants (Fig. 6e,f,i). These results suggested that loss of *Mafb* affects the development of Martinotti cells by disrupting their normal migration choice and, secondarily, disrupting their axonal arborization.

Defective inhibition of pyramidal cells in *Mafb* conditional mutants

We analyzed the functional consequences of the disruption of layer 1 axons in Martinotti cells. To examine the function of SST+ interneurons, we injected AAV viruses engineered to express Channelrhodopsin-2 (ChR2) in SST+ interneurons following Cre-mediated recombination in the somatosensory cortex in control and conditional *Mafb* mutant mice at P2. We then prepared acute slices at P50-60 for whole-cell patch clamp recordings in pyramidal cells. In initial experiments, we found that the minimum LED intensity required to evoke an IPSC was similar between both genotypes (Supplementary Fig. 11h–k). which, together with the lack of difference in intrinsic membrane properties, suggested that both genotypes expressed comparable levels of ChR2. We next used subcellular ChR2 assisted circuit mapping32 to trigger localized synaptic release from SST+ interneuron axons at predefined locations while recording from pyramidal cells. We focused on layer 3 pyramidal cells in order to have sufficient spatial resolution to discriminate between SST+ inputs at different locations within the dendritic arbor of pyramidal cells (Fig. 6j). We found a prominent reduction in IPSC amplitudes in layer 3 pyramidal cells in the mutant *Mafb* slices compared to controls (Fig. 6k,l). These results demonstrated a functional impairment of SST + interneurons in conditional *Mafb* mutant mice.

In vivo functional impairments in *Mafb* conditional mutants

SST+ interneurons exhibit the highest level of orientation selectivity among the different classes of interneurons33,34. Orientation selectivity depends on synaptic inputs, which in

the case of layer 2/3 SST+ interneurons derive primarily from adjacent layer 2/3 pyramidal cells[35,36]. SST+ interneurons in turn influence layer 2/3 pyramidal cells by inhibiting their apical dendrites[37]. Since inhibition from SST+ interneurons modulate the visual tuning properties of pyramidal cells[38], we reasoned that the reduced inhibitory drive observed in conditional *Mafb* mutant mice would likely impact the tuning responses of both pyramidal cells and SST+ interneurons. We measured visually evoked responses in individual neurons using calcium imaging in awake, head-fixed mice (Fig. 7a,b). SST+ interneurons were labeled by injecting conditional adeno-associated viruses (AAV) encoding GCaMP6s into V1 of control and conditional mutant *Mafb* mice. As previously reported[33], we confirmed that layer 2/3 SST+ interneurons respond to drifting gratings and exhibit a broad range of orientation tuning (Fig. 7c). We found similar proportions of SST+ neurons responding to drifting gratings in *Mafb* mutants and controls ($p = 0.709$, Kruskal-Wallis test), indicating that basic functional properties are preserved. This is consistent with the in vitro findings that intrinsic properties of SST+ neurons are not affected in *Mafb* mutants (Supplementary Fig. 11a–g). We then assessed the selectivity of these visual responses. We averaged the stimulus-evoked response (SER) for each drifting grating across all trials and found that the responses evoked by the preferred orientation in conditional *Mafb* mutants were significantly lower (Fig. 7d) and more variable (Fig. 7e) than in controls. We observed no significant differences in orthogonal orientations ($p = 0.063$ and $p = 0.314$, respectively). In line with these observations, we found that the orientation selectivity index (OSI) of SST+ interneurons was significantly lower in conditional *Mafb* mutants compared to controls (Fig. 7f,g). The proportion of selective SST+ interneurons (OSI > 0.25) was also greatly reduced in conditional *Mafb* mutants compared to controls (Fig. 7h).

We then tested the impact of the impaired activity of SST+ interneurons on the visual properties of layer 2/3 excitatory neurons. We used the same experimental approach but labeled all neurons with GCaMP6s and employed an activity-independent marker (tdTomato) to identify SST+ interneurons. Using this approach, we imaged calcium transients in both SST+ and non-SST+ neurons (putative excitatory [pExc] neurons). We found no significant difference in the average orientation selectivity of pExc neurons between controls and conditional *Mafb* mutants ($n = 1321$ and 1424 neurons for controls and mutants, respectively; Kruskal-Wallis test, $p = 0.163$). However, we found significantly higher trial-by-trial variability of evoked responses for all orientations ($n = 1321$ and 1424 neurons for controls and mutants, respectively; Kruskal-Wallis test, $p < 0.05$).

We next evaluated the impact of these single-cell functional impairments on the population-level representations of visual stimuli in V1. By calculating pairwise correlations between all neurons within a single field of view, we determined how strongly the activity of a cell was correlated with that of all other cells in one field of view (Fig. 7i). We found that both SST+ interneurons and pExc neurons display lower pairwise correlations in conditional *Mafb* mutants than in controls (Fig. 7j). Lower pairwise correlations in mutants may reflect differences in information coding of visual stimuli at the population level. To test this idea, we quantified how well neuronal populations represent a visual stimulus in both genotypes by using a decoder[39]. In brief, we used a template-matching decoder to predict which oriented grating was presented to the mouse for each trial. This prediction was calculated from the calcium responses of all cells imaged in a single field of view. The ability of the

decoder to correctly classify the presented grating per trial was significantly lower in conditional *Mafb* mutants than in controls (Fig. 7k) for both SST+ interneurons and pExc neurons (Fig. 7k). These results suggested that population-level representations of visual stimuli are impaired in conditional *Mafb* mutants.

Discussion

Two general principles on the assembly of inhibitory neocortical circuits emerge from our experiments. First, interneuron wiring and function is optimized through a complex sequence of developmental events that begin long before the first synaptic contacts are established. Second, interneurons are fated to develop into specific classes by the time they invade the embryonic cortex. These observations suggest that different classes of interneurons are specified early in development through intrinsic programs that unfold over a protracted period of time.

Optimization of interneuron function through migratory route selection

Interneurons are generated in the subpallium and migrate tangentially to reach the developing cortex40. In spite of their relatively uniform appearance24, migrating interneurons soon segregate in two parallel streams (MZ and SVZ) as they disperse through the embryonic cortex17. Although this seems to be a unique feature of mammalian cortical development18, its impact on neural circuit assembly have remained unclear.

Our results suggest that migratory route selection for cortical interneurons is linked to specific fates. Time-lapse imaging and transplantation experiments revealed that interneurons are committed to particular migratory routes. This suggests that interneurons migrating through the MZ or SVZ express different guidance molecules that contribute to their sorting into specific streams, as shown before for striatal interneurons41. Although previous reports have suggested that migratory route allocation is independent of the place of origin of interneurons20, our experiments reveal that different types of cortical interneurons favor particular routes. For instance, SST+ Martinotti cells migrate preferentially through the MZ, whereas SST+ non-Martinotti cells disperse via the SVZ. Thus, at least for some types of interneurons, route choice is an early decision that must be molecularly encoded in the genetic programs that these cells unfold to reach the cortex. Consistent with this idea, a recent transcriptomic analysis of CGE interneurons suggests that cell identity in this region is also linked to specific route choices42.

The migration of Martinotti cells through the MZ is linked to the development of their axon arbors in layer 1. In contrast to other migrating interneurons43,44, time-lapse imaging experiments revealed that prospective Martinotti cells leave their nascent axon in the marginal zone while they invade the developing cortical plate. This process is highly reminiscent of the development of cerebellar granule cells, which also leave their prospective axons in the molecular layer while migrating from the external granule cell layer to their final position in the cerebellum45. The precise molecular mechanisms linking the migration of Martinotti cells through the MZ and the normal targeting of their axons in layer 1 remain to be identified. It is conceivable that the embryonic MZ creates a permissive

microenvironment for early synaptic stabilization, perhaps with the participation of Cajal-Retzius cells that are known to shape the architecture of layer 146.

We found that MafB is an important factor controlling the migration of Martinotti cells through the MZ, although other molecules are likely involved. Our experiments revealed that only Martinotti cells that fail to migrate through the MZ have very poorly developed axonal in layer 1, which suggest that migratory route is linked to axonal targeting. Although we cannot exclude other roles for MafB, our results indicate that abnormal development of axonal arbors in layer 1 impacts their ability to regulate the function of pyramidal cells. Considering the prominent role of Martinotti cells in neural circuits in the visual cortex35–38, the findings of (i) a deficit in SST+ axonal arborization in layer 1, (ii) a reduction in inhibition in layer 2/3 pyramidal neurons, and (iii) impaired tuning of visual responses are all consistent with each other, indicate that defects in a subset of Martinotti cells disrupt population-level representations of visual stimuli.

Early fate specification of distinct types of cortical interneurons

Several models have been proposed to explain the mechanisms underlying the diversity of cortical interneurons. One model proposes that interneuron identity is established shortly after cells become postmitotic11, even though many of the characteristics that distinguish a particular type of interneuron are not evident until adulthood. Implicit to this model is that a limited number of genetic factors are necessary to prime the development of newborn cells toward a particular fate47,48. Alternatively, the genetic information for cellular identity of a particular type of interneuron is only acquired once the cells arrive to their final position in the cortex19. In this model, newborn interneurons acquire a potentially uniform intrinsic program, only segregating into general or 'cardinal' classes. The specification of particular cell types would then require their interaction with the cortical environment, possibly through activity-mediated mechanisms49.

Our results strongly support the hypothesis that cells are fated to become specific types of cortical interneurons very early in development. Using layer 2/3 SST+ interneurons as a model, we found that cells within this main group of interneurons are specified to become either Martinotti or non-Martinotti cells at least by the time they choose a migratory route to invade the embryonic cortex. Several lines of evidence support this conclusion. First, many of the genes that distinguish SST+ cells during their migration are enriched in specific types of SST+ interneuron in the adult cortex7,8, a strong indication that cell identity is established molecularly before morphological and electrophysiological properties emerge. Second, targeted electroporation of the MZ revealed that the vast majority of SST+ cells migrating through this route become Martinotti cells, which implies that non-Martinotti cells migrate through the SVZ. Third, despite the layer 1 axonal defects, Martinotti cells that fail to migrate through the MZ in conditional *Mafb* mutants retain molecular (CR and CB co-expression) and electrophysiological (intrinsic properties) features of Martinotti cells, which suggests that they are specified prior to interacting with local cues in the MZ. Consistent with this idea, a recent single-cell RNA-seq study have shown that different groups of SST+ interneurons can be readily identified shortly after birth in the ganglionic eminences50. Additional experiments would be nevertheless required to unequivocally demonstrate that

Martinotti and non-Martinotti SST+ interneurons are specified prior to their arrival in the cortex. In any case, our results demonstrate that fate potential, at least for distinct subtypes of SST+ interneurons, precedes the emergence of distinctive interneuron properties.

Methods

Mice

The following transgenic mouse lines were used in this study: *Ai9*[B6.Gt(ROSA)26Sor^tm9(CAG-tdTomato)Hze]51, *Calb2^Cre* [B6(Cg)-Calb2tm1(cre)Zjh]52, *Dlx1/2-CreERT2* [Tg(I12b-cre/ERT2,-ALPP)37Fsh]53, *Elfn1*54, *Gad65-Gfp*55, *Mafb^fl/fl* 56, *Neto1* [B6N.129-Neto1^tm1Mci]57, *Nkx2-1-Cre* [C57BL/6J-Tg(Nkx2-1-Cre)2Sand]27, *Nkx2-1^CreERT2*[Nkx2-1tm1.1(cre/ERT2)Zjh]52, *RCE* [(B6.Gt(ROSA)26Sor^tm1.1(CAG-EGFP)Fsh]58, *Sst^Cre* [B6N.Cg-Ssttm2.1(cre)Zjh]52 and *Vgat^Cre* [B6.FVB-Tg(Slc32a1-cre)2.1Hzo] 59. All adult mice were housed in groups and kept on reverse light/dark cycle (12/12 h) regardless of genotypes. Only time-mated pregnant female mice that have undergone in utero surgeries were house individually. Both male and female mice were used in all experiments. For developmental and histology studies, mice ages range from E14.5 to P30. For electrophysiology, mice ages range from P20-P28 for intrinsic properties recordings and P50-P60 for optogenetic stimulation. For in vivo two-photon imaging studies, mice ages range from P62-P75 at the time of imaging. All procedures were approved by the Instituto de Neurociencias, King's College London and University of Edinburgh animal welfare committees and were performed under UK Home Office project licenses.

Histology

For in situ hybridization, embryonic mice were perfused transcardially with 4% paraformaldehyde (PFA) in PBS treated with DEPC, and the dissected brains were fixed overnight at 4°C in the same solution. Brains were embedded in 4% low melting agarose and sectioned at 60 μm with a vibratome. Free-floating coronal sections were mounted on superfrost slides and subsequently hybridized with digoxigenin-labeled probes, as described before47.

For immunohistochemistry, postnatal mice were perfused transcardially with 4% PFA in PBS and the dissected brains were fixed for 2 h at 4°C in the same solution. Brains were sectioned at 60 μm on a vibratome or 40 μm on a freezing microtome and free-floating coronal sections were then subsequently processed for immunohistochemistry as previously described60. Embryonic mice were dissected and fixed overnight in 4% PFA in PBS. Brains were sectioned at 100 μm (E13.5 to E15.5) or 60 μm (E16.5 to E17.5) on a vibratome. Free-floating coronal sections were processed for immunohistochemistry as previously described60. Postnatal mice were perfused transcardially with PBS followed by 4% PFA and post-fixed for 3 h. Sucrose cryoprotected brains were sectioned coronally at 60 μm (for cell density quantifications) or 120 μm (for axonal arborization) on a freezing microtome, and free-floating sections were used for immunohistochemistry.

All primary antibodies used in this study were previously published: chicken-anti-GFP (1:1000 Aves Lab)[52], rabbit-anti-DsRed (1:500, Clonetech)[52], rat-anti-Somatostatin (1:200, Millipore)[52], mouse-anti-Parvalbumin (1:2000, Swant)[52], rabbit-anti-Calretinin (1:1000, Swant)[52], rabbit-anti-Calbindin (1:1000, Swant)[52], rabbit-anti-Tbr2 (1:500, Abcam)[61], Rabbit-anti-MafB (1:500, Atlas antibody)[56]. Secondary antibodies (Molecular Probes) were conjugated with Alexa Fluor dyes and used at 1:500: Anti-Chicken Iggy (H+L) 488, Anti-Mouse IgG1 647, Anti-Rat IgG (H+L) 488, Anti-Rat IgG (H+L) 546, Anti-Rabbit IgG (H+L) 555, Anti-Rabbit IgG (H+L) 488.

Cloning

Overexpression plasmids, *RV-CAG-dio-Kikume*, *RV-CAG-dio-mtdTomato*, *RV-CAG-dio-mEYFP*, *RV-CAG-dio-Kif5C 560-P2A-mtdTomato* were cloned by PCR or overlapping PCR into a conditionally expressing retroviral backbone (Addgene 87662) using AscI and PacI as cloning sites. *Kif5C 560* sequences were amplified by using *pBa-KIF5C 599-tdTomato-FKBP*, a gift from Gary Banker (Addgene plasmid 64211)[62]. In situ hybridization probes *T7T3-PacI-Mafb*, *T7T3-pacI-Neto1*, and *T7T3-PacI-Elfn1-459-1199* were cloned from E17.5 mouse forebrain cDNA library by PCR amplification followed by restriction digestion.

Slice experiments

E13.5 to P1 animals were perfused with 5 ml of ice-cold sucrose solution (70 mM sucrose, 86 mM NaCl, 4 mM KCl, 1 mM NaH$_2$PO$_4$, 7 mM MgCl$_2$, 26mM NaHCO$_3$, 25 mM glucose, 0.5 mM CaCl$_2$). Cortices were dissected and embedded in 4% low melting agarose in PBS. Upon solidification of the agar block, the brain-agarose block was glued onto a vibratome and cut in ice-cold sucrose solution at 250 μm. Slices were transferred into an ice-cold solution of KREB to recover for 15 min before being placed into a Millicell insert well (Millipore) and incubated at 37ºC in 5% CO$_2$ with MEM/10% FBS/1% Penstrep. After 1 h at 37ºC, slice medium was changed to Neurobasal/B27. Slices were incubated in Neurobasal/B27 for up to 1 week without any changing of medium.

RNA sequencing

The cortex of E16.5 or E17.5 animals was dissected in ice-cold HBSS (with 25 mM of Glucose) and flat-mounted onto a flat 1% agar block in HBSS-glucose in a 60 mm petri dish, with the lateral cortex towards the agar. Excessive HBSS solution around the flat-mounted tissue was dried off using Whatman filter paper no 9 (Sigma-Aldrich Z274852). Melted 1% PBS agar solution cooled to 42°C was poured on the petri dish containing the flat mounted tissue, covering the entire remaining volume of the dish and flat mounted using the lid of the dish. Upon solidification of the agar block, with the lateral cortex facing upwards, the block was glued onto a vibratome and cut in ice-cold sucrose solution at 120 μm from the pial surface. Based on pilot experiments, the 1st tissue section was considered the MZ and the 4th or 5th section was considered the SVZ in E16.5 and E17.5 embryos, respectively.

Slices were digested for 20 min at 37°C with 0.1 mg/ml PronaseE (Sigma), dissociating solution containing 1 mg/ml of Trehalose, 20 mM glucose, 0.8 mM kynurenic acid, 0.05

mM APV, 0.09M Na_2SO_4, 0.03M K_2SO_4 and 0.014M $MgCl_2$. During digestion, the solution was oxygenated by bubbling 5% carbogen (95% O2/5% CO_2). After digestion, cells were washed 3 times with ice-cold OptiMem (Life Technologies, Gaithersburg, MD) containing 20 mM glucose, 0.4 mM kynurenic acid, 0.025 mM APV, and mechanically dissociated by trituration with a P1000 pipette. TdTomato+ cells were isolated using fluorescence-activated cell sorting (FACS) with a flow cytometer (Becton Dickinson), and collected directly in 350 μl of RLT buffer of the RNeasy micro kit (Qiagen). Collected cells were stored at -80°C and RNA was later isolated using the RNeasy micro kit following the manufacturer's specifications. Approximate 0.5-1 ng of total RNA was recovered for 15,000 cells. Low input RNA sequencing was performed by HudsonAlpha Genomic Service Lab (Huntsville, Alabama), using standard sequencing conditions of 50-100 bp paired-end and 50M reads.

Viral infections

Retroviruses were produced as described previously[63]. In brief, HEK293FT cells were plated at 10^6 cells per well in six 15 cm plates. Upon 70-80% confluence, cells were transfected with retroviral constructs (*pRV-CAG-dio-mtdTomato*, *pCMV-Vsv-g*, and *pCMV-GAG-pol*) using TransIt reagent (Mirus, Madison WI). Forty-eight hours post transfection, 120 ml of supernatant were concentrated by two rounds of ultracentrifugation and re-suspended in 80 μl of PBS and stored in 5 μl aliquots at -80°C. Typical virus titers range from $1-5 \times 10^8$ IU/ml. The adeno-associated viruses (AAVs) used in this study were acquired from the University of Pennsylvania Vector Core (USA).

In utero viral infection was performed on E12.5 or E14.5 embryos. Pregnant females were anesthetized with 2.5% isoflurane and the abdominal cavity cut to expose the uterus. For each embryo, about 200 nl of concentrated retrovirus ($\sim 10^8$ IU/ml) were injected into the lateral ventricle of the telencephalon using a glass capillary needle. The uterine horns were then placed back in the abdominal cavity, suture closed, and the female was placed in 32°C recovering chamber for 1 h post-surgery.

Pial surface electroporation

Targeting of cells close to the pial surface was performed as described previously[26]. In brief, P0 pups were anesthetized with 4.5% isoflurane and head fixed on a stereotaxic stage. A volume of 500-800 nl containing 1.5 μg/μl plasmids (*pRV-CAG-dio-mEYFP* or *pCAG-dio-Kif5C 560-EYFP-P2A-mtdTomato*) was injected 0.5 μm below the skull equidistant from lambda and the visual eye bulge using a glass capillary needle. A 5 mm diameter electrode was oriented towards the ventral side and square electric pulses of 95 V and 50 ms were passed through the pups five times, spaced 950 ms, using a pulse electroporator. Each pup was the placed on a recovering chamber at 37°C for 30 min and then returned to their mother for nursing.

Time-lapse imaging

Slice were kept at 37°C and 5% CO_2 for the duration time-lapse. For photoconversion experiments, a plasmid encoding conditionally expressing Kikume (RV-CAG-dio-Kikume) was electroporated in the MGE of slices obtained from E13.5 *Nkx2-1-Cre* embryos. Two days after electroporation, Kikume-expressing cells in the MZ were visualized with a high

magnification objective (40x NA 0.9, Leica) on an inverted confocal microscope (SP2, Leica). Regions of interest were drawn manually around the soma of 10-12 cells per slice, and photoconversion was achieved by using 3 by 3 average line scan with a 405 nm laser set at 10 mW. Converted cells were verified by emission from GFP to RFP. Time-lapse images were taken at intervals of 2 h per frame for a total of 16 h using a 10x objective. At each time point, 4-5 fields of view were acquired with a z-stack interval of 10 μm, spanning 100 μm to cover both the dorsal and ventral telencephalon.

For early postnatal time-lapse imaging, time-mated E14.5 female from $Nkx2-1^{CreER};Ai9$ was injected with single dose of 2mg/kg of tamoxifen diluted in corn oil intraperitoneally. At P0-P1, brains from either $Nkx2-1^{CreER};Ai9$ or $Dlx1/2^{CreER};Ai9$ neonate mice were cut in 250 μm thick coronal slices in HBSS and cultured on Millicell (Millipore) organotypic membrane inserts in Neurobasal/B27. Slices were kept at 37°C and 5% CO2 for 6 h to settle before imaging. Time-lapse images were taken at intervals of 1 to 1.5 h per frame for 60-70 h using a 25x water immersion objective (NA 0.95) in an inverted confocal resonant scanner couple with a hybrid photon counting detector (SP8, Leica). At each time point, the acquired image includes the cortical plate and the pial surface with z-stack interval of 1.25 μm, spanning 60-70 μm.

Electrophysiology

For the analysis of intrinsic properties, P20-P23 mice from $Sst^{Cre};Mafb^{fl/+};RCE$ and $Sst^{Cre};Mafb^{fl/fl};RCE$ were deeply anesthetized with sodium pentobarbital and transcardially perfused with 10 ml ice-cold cutting sucrose solution (in mM: 87 NaCl, 11 Glucose, 75 Sucrose, 2.5 KCl, 1.25 NaH_2PO_4, 0.5 $CaCl_2$, 7 $MgCl_2$, 26 $NaHCO_3$, oxygenated with 95% O_2/5% CO_2). Following decapitation, the brain was quickly removed and glued to a cutting platform before being submerged in ice-cold sucrose solution. Coronal slices (300 μm) were cut using a vibratome (Leica) and placed in cutting artificial cerebrospinal fluid (ACSF) (in mM: 124 NaCl, 1.25 NaH_2PO_4, 3 KCl, 26 $NaHCO_3$, 10 Glucose, 2 $CaCl_2$, 1 $MgCl_2$, oxygenated with 95% O_2/5% CO_2) at 32°C for 1 h, and then kept at room temperature for recording.

Cells were visualized with an upright microscope (Olympus). Patch pipettes (3-5 MΩ) were made from borosilicate glass capillaries using a vertical puller (P10, Narishige) and filled with intracellular solution containing (in mM) 5 KCl, 130 K-Gluconate, 10 HEPES, 2.5 $MgCl_2$, 4 Na_2ATP, 0.4 Na_3GTP, 10 Na-Phosphocreatine, 0.6 EGTA (pH 7.2-7.3, 285-295 mOsm) for current clamp, and (in mM)115 $CsMeSO_3$, 20 CsCl, 10 HEPES, 2.5 $MgCl_2$, 4 Na_2ATP, 0.4 NaGTP, 10 Na-Phosphocreatine, 0.6 EGTA (pH 7.2-7.3, 285-295 mOsm) for voltage clamp. Intracellular solutions also contained 0.2% neurobiotin (Vector Laboratories, United Kingdom). Traces were recorded using a Multiclamp 700B amplifier (Molecular Devices, United Kingdom), sampled at 20 kHz and filtered at 3 kHz. Cells were excluded from analysis if the access resistance exceeded 25 MΩ.

For subcellular ChR2 assisted circuit mapping (sCRACM), P2 $Sst^{Cre};Mafb^{fl/+}$ or $Sst^{Cre};Mafb^{fl/fl}$ mice were anaesthetized with isoflurane and injected in the somatosensory cortex with AAV9-Ef1a-dio-ChETA(E123T/H134R)-eYFP-WPRE-hGH (three rostral to caudal 200 nl injections separated 100 μm and at 300 μm depth from the cortical surface).

Injected mice were deeply anesthetized with sodium pentobarbital at P50-P60 and transcardially perfused with 10ml ice cold N-Methyl-D-Glucamine NMDG-ACSF (in mM: 93 NMDG, 2.5 KCl, 1.2 NaH_2PO_4, 30 $NaHCO_3$, 20 HEPES, 25 glucose, 5 Sodium ascorbate, 2 thiourea, 3 sodium pyruvate, 10 $MgSO_4$, 0.5 $CaCl_2$ [pH 7.3] oxygenated with 95% O_2 and 5% CO_2). Following decapitation, the brain was quickly removed and glued to a cutting platform before being submerged in ice cold NMDG-ACSF. Parasagittal slices (300 μm) were cut using a vibratome (Leica) and placed in NMDG-ACSF at 32°C for 15 min and then kept at room temperature ACSF until recording. Recording ACSF was supplemented with tetrodotoxin (TTX, 1μM, Tocris) and 4-aminopyridine (4-AP, 100μM, Alomone Labs, Israel). Experiments were performed in voltage clamp. After establishing a whole cell recording, the cell was left for 3 min before recording. LED and laser stimulation were applied via a 10x objective (0.25 NA, Olympus). First, cells were stimulated with decreasing LED-intensities from 100% (75 mW/mm^2) from a cool LED light source (473 nm, 10 sweeps per intensity at 0.1Hz), and minimal response intensity was assessed in 1% steps. Laser illumination spots were stimulated in a pseudo-randomized 7 by 6 grid spaced 100 μm. The first row was positioned in the middle of layer 1, and the cell body of the recorded cell was aligned with column 3, 4 or 5. The stimulation spot size was approximately 60 μm in diameter as assessed by a line scan over the apical dendrites of a layer 5 pyramidal cell following a protocol described earlier[32]. Photo-stimulation was achieved by 1ms pluses with a 473 nm laser at 0.14 mW/mm^2 (Rapp Optoelectronic, Germany). Each photo-stimulation was repeated 3 times. After recording, slices were fixed for 1 h at room temperature in 4% PFA. Recorded cells were visualized with streptavidin staining and were excluded from the analysis if the apical dendrite was cut.

In vivo two-photon imaging

Adeno-associated viral (AAVs) injections and cranial window implantations were performed as previously described[64]. In brief, mice were anaesthetized with isoflurane, and AAVs were injected in V1 at three different depths (~250, 400, and 600 μm from cortical surface; 50 nl per site). We used AAV1-Syn-Flex-GCaMP6s-WPRE-SV40 to label SST+ interneurons (4 $Sst^{Cre};Mafb^{fl/+}$ and 4 $Sst^{Cre};Mafb^{fl/fl}$ mice) as well as AAV1-Syn-GCaMP6s-WPRE-SV40 and AAV1-CAG-Flex-tdTomato-WPRE-bGH to label SST+ interneurons and putative excitatory neurons (4 mice per genotype). Two weeks after AAV injection, a craniotomy (around 2x2 mm) was made over the left V1 (centered 3 mm lateral and 1 mm anterior to lambda). We then sealed the craniotomy by fixing a glass cover slip with cyano-acrylic glue. Finally, a custom-built head-post was implanted on the skull using glue and dental acrylic.

Two-photon imaging and visual stimulation were performed as previously described[64]. In brief, we used a custom-built resonant scanning two-photon microscope with a 25x objective (XL PlanN 25x 1.05 WMP, Olympus). Excitation light was produced by a Ti:Sapphire pulsed laser (Chameleon Vision-S, Coherent, USA; < 70 fs pulse width, 80 MHz repetition rate) tuned to 920 nm. We acquired 600×600 pixel images with a field of view of 350x350 μm at 40 frames/s, at cortical depths between 130–350 μm. Laser power at the brain surface was kept below 50 mW. Habituation and imaging started 2 weeks after AAV injection. Mice were habituated to head-fixation in the dark for 45 min. Visual stimuli were presented on an LCD monitor (51×29 cm, Dell, UK) positioned at 20 cm from the right eye, covering

104°×72° of the visual field. Visual stimulation trials included the presentation of an isoluminant grey screen (5 s) followed by stationary full-field square-wave gratings (2 s) and the corresponding drifting phase for 2 s (0.05 cpd, 1.5 Hz, 8 equally spaced directions in randomized order, contrast 80%, mean luminance 37 cd/m^2). The drift direction was perpendicular to the gratings orientation. We acquired 10-15 trials for each imaging field of view.

Quantification: Histology

Images were taken using fluorescence microscopes (DM5000B, CTR5000 and DMIRB from Leica or Apotome.2 from Zeiss) coupled to digital cameras (DC500 or DFC350FX, Leica; OrcaR2, Hamamatsu with the appropriate emission filter sets or in inverted confocal microscopes (Leica TCS SP8 and Zeiss LSM800 Airyscan). Images stained with reporter proteins (GFP or DsRed) or specific markers were quantified using customized software written in MATLAB (Mathworks, see code availability below). In brief, cell body were segmented using disk morphological shape function, size, and intensity thresholding. Background and high-density noise were removed via filtering. Anatomical regions such as the MZ, CP, and SVZ were determined using DAPI counterstaining and defined as regions of interest (ROI). Each animal was considered a biological replicate. For each brain, 10-12 images spanning rostral to caudal regions of the somatosensory cortex were taken and treated as technical replicates.

For quantification of axonal length, the maximum projection of z-stack images of single cells stained with fluorescent protein markers was quantified using a customized script written in MATLAB (Mathworks). For each z-projection, axons, soma and dendrites were segmented by setting a low intensity threshold, and soma and dendrites were segmented by setting a high intensity threshold. The resulting axonal binary image was achieved by subtracting the low intensity threshold to the high intensity threshold images. Binary pixels were converted to total axonal length and anatomical boundaries of cortical layers were determined by DAPI counterstaining and defined as ROIs.

Quantification: RNAseq analysis

RNAseq data from MZ and SVZ FACS cells were mapped to mouse genome version mm9 (USCD), and count data were analyzed with Bioconductor software DESeq2 in R. False discovery rate (FDR) was set at 5% using Benjamini-Hochberg method. Differentially expressed genes between MZ and SVZ with average log FPKM values > 5 were plotted into heatmap using normalized row z-score in R.

Quantification: Time-lapse imaging analysis

Time-lapse images were analyzed using ImageJ Mtrack2 plugin. For photoconversion experiments, only Kikume-R (converted) cells were tracked. For experiment assessing neurites at the MZ, only cells that have entered the cortical plate and stayed in focus throughout the entire time series were analyzed. We used the maximum projection of z-stack images to manually trace the location of the soma and neurite tips and their respective speed and distances were computed.

Quantification: Electrophysiology

Intrinsic properties were recorded in current clamp and analyzed using Clampfit 10.7 (Molecular Devices, United Kingdom). The membrane potential was assessed directly after establishing a whole cell recording. Afterwards, the membrane potential was biased to -70 mV for subsequent recordings. Input resistance was calculated from 5 increasing 5 pA 500 ms current steps. Sag was assessed from the average membrane potential at the end of a 500 ms current pulse initially hyperpolarizing the cell to -100 mV. Rise-time and decay-time were calculated from the 10%-90% and 90%-10% amplitudes, respectively. fAHP was calculated as the difference between AP threshold and the maximum hyperpolarized value before reaching the AP threshold potential. Rheobase was calculated from 1pA steps. Maximum firing frequency was calculated form 100 pA steps. After recording, slices were fixed for 1h at RT in 4% paraformaldehyde. Recorded cells were visualized with streptavidin staining and were included if axonal projections extended into layer 1, confirming their Martinotti identity.

For sCRACM, analyses were done with using customized software written in MATLAB (Mathworks). Responses were analyzed as the average response amplitude of the three repeats if a response was detected in at least 2 sweeps. Attenuation correction was applied. Attenuation, $1/g(r)$, was estimated as $1/g(r) = 1-2(-r/\lambda)$, where r is the distance from the soma of the stimulated spot32. We used $\lambda = 365$, as has been reported previously for Cesium-based intracellular solutions65.

Quantification: In vivo two-photon imaging analysis

Imaging data were corrected for motion artifacts by using Discrete Fourier transformation-based image alignment (SIMA 1.3.2, sequential image analysis)66. Neuronal cell bodies were selected manually based on down-sampled frames (2 Hz), as well as maximum intensity projections for each trial. Fluorescence traces were calculated as the mean pixel intensity for each cell soma. F/F_0 traces were generated and corrected for local neuropil contamination using the FISSA toolkit, as previously described64,67. We calculated stimulus evoked responses (SER) for each neuron for each trial by taking the mean F/F_0 during each 2 s drifting grating (R_{drift}) and the mean F/F_0 during the last 2 s of the previous grey period (R_{grey}) and calculating an index:

$$SER = \frac{\left(R_{drift} - R_{grey}\right)}{\left(R_{drift} + R_{grey}\right)}$$

The variability across trials was calculated for each drifting period as the standard error of the mean (SEM) of the SER across all trials. The preferred orientation (SER_{pref}) was defined for each neuron by calculating the average F/F_0 for both drifting directions of each orientation and by taking the orientation with the maximum SER value. Orientation tuning was quantified by calculating an orientation selectivity index (OSI, difference between SER_{pref} and $SER_{orth,}$ where SER_{orth} is the average response to the orientation orthogonal to the preferred one).

The correlation coefficient of two neurons is a measure of their linear dependence. For each field of view with N neurons, we calculated the Pearson correlation coefficient defined as,

$$\rho(A, B) = \frac{1}{N-1} \sum_{i=1}^{N} \left(\frac{A_i - \mu_A}{\sigma_A} \right) \left(\frac{B_i - \mu_B}{\sigma_B} \right),$$

where μ_A and σ_A are the mean and standard deviation of neuron A, respectively, and μ_B and σ_B are the mean and standard deviation of neuron B. The pairwise correlation coefficient matrix of all neurons is then the matrix of correlation coefficients for each pairwise variable combination.

To quantify the accuracy by which the four orientations could be classified based on the neuronal population activity, a template-matching decoder was employed, which compares the population activity to response templates of the different stimulus types[39]. These templates are generated by taking the mean F/F$_0$ across trials during the presentation of each oriented grating (θ) for each neuron in a single field of view, resulting in a template of population activity. The similarity of this template (R^θ) to the actual population activity (R^{stim}) is given by:

$$I_\theta = R \frac{\sum_{i=1}^{N} R_i^{stim} \cdot R_i^\theta}{\left| R^\theta \right| \cdot \left| R^{stim} \right|},$$

where i indexes the N elements (neurons) of R. The similarity index I is calculated for all orientations and the decoded output is determined by taking the orientation with the highest similarity to the population activity. Decoder accuracy is given by the percentage of correctly decoded trials.

Statistical analysis

Error bars in all graphs indicate standard error of the mean (SEM) unless otherwise stated in the legends. For each experiment, the sample size and statistical tests used are summarized in Supplementary Table 1. No statistical methods were used to pre-determine sample sizes but our sample sizes are similar to those reported in previous publications[23, 53, 55, 56, 60, 64]. Mice were numbered randomly and selected sequentially. With the exception of time-lapse experiments, data collection and analysis were not performed blind to the conditions of the experiments. All other imaging and physiology data were collected with a reference number, with the experimentalist blinded to the genotype. Data analyses were performed in MatLab and R with custom-written code, and sample genotype information was compiled at the end of analysis. For all parametric statistical tests, data were tested for normality with Shapiro-Wilk's test and equal variances using F-test. No data point was excluded in the study.

Life Sciences Reporting Summary

Further information on experimental design is available in the Life Sciences Reporting Summary.

Code availability

Custom-written codes in MATLAB (Mathworks, USA) and R are available and accessible via public web based servers. Live versions of all codes can be found on GitHub. The package for in vivo calcium imaging analysis can be located at https://github.com/rochefort-lab/fissa. The codes used to generate and analyze sCRACM and histological images can be located in the corresponding folders at https://github.com/OscarMarinlab/Papers/tree/master/Lim2018/Figures_codes/Matlab_scripts.

Data availability

Data supporting the findings of this study are available along with its corresponding analysis code at https://github.com/OscarMarinlab/Papers/tree/master/Lim2018/Figures_codes. Raw RNA-sequencing data and the analysis pipeline used in this study are available at the NCBI/GEO server with accession numbers GSE111150.

Supplementary Material

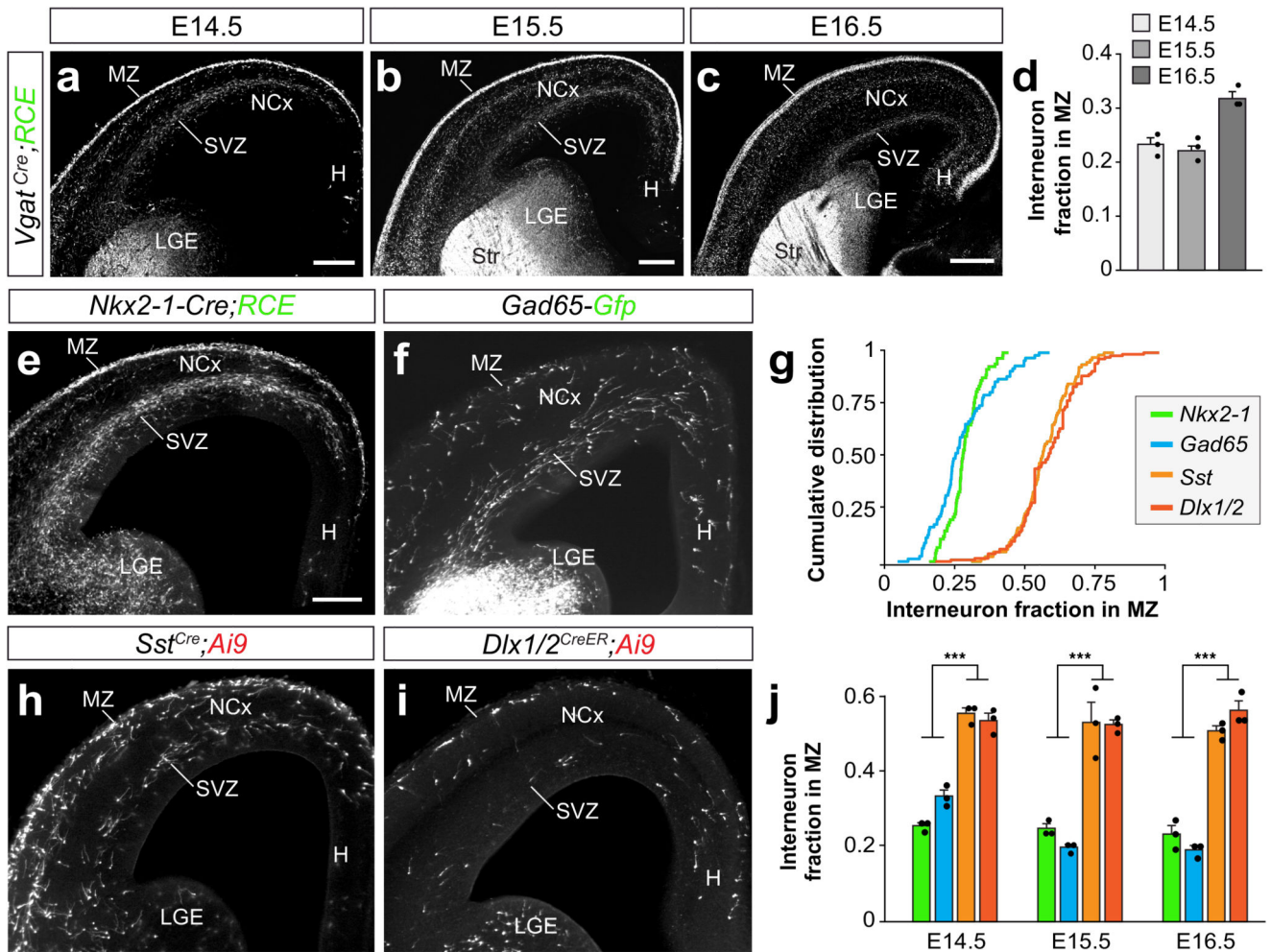Refer to Web version on PubMed Central for supplementary material.

Acknowledgements

References

1. Tomioka N, et al. Neocortical origin and tangential migration of guidepost neurons in the lateral olfactory tract. J Neurosci. 2000; 20:5802–5812. [PubMed: 10908621]

2. Shu T, Li Y, Keller A, Richards LJ. The glial sling is a migratory population of developing neurons. Development. 2003; 130:2929–2937. [PubMed: 12756176]

3. López-Bendito G, et al. Tangential neuronal migration controls axon guidance: a role for Neuregulin-1 on thalamocortical axon navigation. Cell. 2006; 125:127–142. [PubMed: 16615895]

4. Niquille M, et al. Transient neuronal populations are required to guide callosal axons: a role for semaphorin 3C. PLoS Biol. 2009; 7:e1000230. [PubMed: 19859539]

5. Nikolaou N, Meyer MP. Lamination speeds the functional development of visual circuits. Neuron. 2015; 88:999–1013. [PubMed: 26607001]

6. Tremblay R, Lee S, Rudy B. GABAergic interneurons in the neocortex: From cellular properties to circuits. Neuron. 2016; 91:260–292. [PubMed: 27477017]

7. Zeisel A, et al. Cell types in the mouse cortex and hippocampus revealed by single-cell RNA-seq. Science. 2015; 347:1138–1142. [PubMed: 25700174]

8. Tasic B, et al. Adult mouse cortical cell taxonomy revealed by single cell transcriptomics. Nat Neurosci. 2016; 19:335–346. [PubMed: 26727548]

9. Ascoli GA, et al. Petilla terminology: nomenclature of features of GABAergic interneurons of the cerebral cortex. Nat Rev Neurosci. 2008; 9:557–568. [PubMed: 18568015]

10. Klausberger T, Somogyi P. Neuronal diversity and temporal dynamics: the unity of hippocampal circuit operations. Science. 2008; 321:53–57. [PubMed: 18599766]

11. Wonders CP, Anderson SA. The origin and specification of cortical interneurons. Nat Rev Neurosci. 2006; 7:687–696. [PubMed: 16883309]

12. Kawaguchi Y, Kubota Y. Physiological and morphological identification of somatostatin- or vasoactive intestinal polypeptide-containing cells among GABAergic cell subtypes in rat frontal cortex. J Neurosci. 1996; 16:2701–2715. [PubMed: 8786446]

13. Wang Y, et al. Anatomical, physiological and molecular properties of Martinotti cells in the somatosensory cortex of the juvenile rat. J Physiol. 2004; 561:65–90. [PubMed: 15331670]

14. Ma Y, Hu H, Berrebi AS, Mathers PH, Agmon A. Distinct subtypes of somatostatin-containing neocortical interneurons revealed in transgenic mice. J Neurosci. 2006; 26:5069–5082. [PubMed: 16687498]

15. Xu H, Jeong HY, Tremblay R, Rudy B. Neocortical somatostatin-expressing GABAergic interneurons disinhibit the thalamorecipient layer 4. Neuron. 2013; 77:155–167. [PubMed: 23312523]

16. Gelman DM, Marín O. Generation of interneuron diversity in the mouse cerebral cortex. Eur J Neurosci. 2010; 31:2136–2141. [PubMed: 20529125]

17. Tanaka DH, Nakajima K. Migratory pathways of GABAergic interneurons when they enter the neocortex. Eur J Neurosci. 2012; 35:1655–1660. [PubMed: 22639844]

18. Tanaka DH, Oiwa R, Sasaki E, Nakajima K. Changes in cortical interneuron migration contribute to the evolution of the neocortex. Proc Natl Acad Sci USA. 2011; 108:8015–8020. [PubMed: 21518872]

19. Wamsley B, Fishell G. Genetic and activity-dependent mechanisms underlying interneuron diversity. Nat Rev Neurosci. 2017; 18:299–309. [PubMed: 28381833]

20. Miyoshi G, Fishell G. GABAergic interneuron lineages selectively sort into specific cortical layers during early postnatal development. Cereb Cortex. 2011; 21:845–852. [PubMed: 20732898]

21. Villette V, et al. Development of early-born gamma-aminobutyric acid hub neurons in mouse hippocampus from embryogenesis to adulthood. J Comp Neurol. 2016; 524:2440–2461. [PubMed: 26779909]

22. Nowotschin S, Hadjantonakis AK. Use of KikGR a photoconvertible green-to-red fluorescent protein for cell labeling and lineage analysis in ES cells and mouse embryos. BMC Dev Biol. 2009; 9:49. [PubMed: 19740427]

23. Marín O, Valdeolmillos M, Moya F. Neurons in motion: same principles for different shapes? Trends Neurosci. 2006; 29:655–661. [PubMed: 17046074]

24. Martini FJ, et al. Biased selection of leading process branches mediates chemotaxis during tangential neuronal migration. Development. 2009; 136:41–50. [PubMed: 19060332]

25. Hilscher MM, Leao RN, Edwards SJ, Leao KE, Kullander K. Chrna2-Martinotti cells synchronize layer 5 type A pyramidal cells via rebound excitation. PLoS Biol. 2017; 15:e2001392. [PubMed: 28182735]

26. Breunig JJ, et al. Rapid genetic targeting of pial surface neural progenitors and immature neurons by neonatal electroporation. Neural Development. 2012; 7:26. [PubMed: 22776033]

27. Xu Q, Tam M, Anderson SA. Fate mapping Nkx2.1-lineage cells in the mouse telencephalon. J Comp Neurol. 2008; 506:16–29. [PubMed: 17990269]

28. Buchanan KA, et al. Target-specific expression of presynaptic NMDA receptors in neocortical microcircuits. Neuron. 2012; 75:451–466. [PubMed: 22884329]

29. Bortone DS, Olsen SR, Scanziani M. Translaminar inhibitory cells recruited by layer 6 corticothalamic neurons suppress visual cortex. Neuron. 2014; 82:474–485. [PubMed: 24656931]

30. Jacobson C, Schnapp B, Banker GA. A change in the selective translocation of the Kinesin-1 motor domain marks the initial specification of the axon. Neuron. 2006; 49:797–804. [PubMed: 16543128]

31. Xu X, Roby KD, Callaway EM. Mouse cortical inhibitory neuron type that coexpresses somatostatin and calretinin. J Comp Neurol. 2006; 499:144–160. [PubMed: 16958092]

32. Petreanu L, Mao T, Sternson SM, Svoboda K. The subcellular organization of neocortical excitatory connections. Nature. 2009; 457:1142–1145. [PubMed: 19151697]

33. Ma WP, et al. Visual representations by cortical somatostatin inhibitory neurons--selective but with weak and delayed responses. J Neurosci. 2010; 30:14371–14379. [PubMed: 20980594]

34. Cottam JC, Smith SL, Hausser M. Target-specific effects of somatostatin-expressing interneurons on neocortical visual processing. J Neurosci. 2013; 33:19567–19578. [PubMed: 24336721]

35. Adesnik H, Bruns W, Taniguchi H, Huang ZJ, Scanziani M. A neural circuit for spatial summation in visual cortex. Nature. 2012; 490:226–231. [PubMed: 23060193]

36. Jiang X, et al. Principles of connectivity among morphologically defined cell types in adult neocortex. Science. 2015; 350:aac9462. [PubMed: 26612957]

37. Pfeffer CK, Xue M, He M, Huang ZJ, Scanziani M. Inhibition of inhibition in visual cortex: the logic of connections between molecularly distinct interneurons. Nat Neurosci. 2013; 16:1068–1076. [PubMed: 23817549]

38. Adesnik H. Synaptic mechanisms of feature coding in the visual cortex of awake mice. Neuron. 2017; 95:1147–1159. [PubMed: 28858618]

39. Montijn JS, Vinck M, Pennartz CM. Population coding in mouse visual cortex: response reliability and dissociability of stimulus tuning and noise correlation. Front Comput Neurosci. 2014; 8:58. [PubMed: 24917812]

40. Marín O, Rubenstein JLR. A long, remarkable journey: tangential migration in the telencephalon. Nat Rev Neurosci. 2001; 2:780–790. [PubMed: 11715055]

41. Marín O, Yaron A, Bagri A, Tessier-Lavigne M, Rubenstein JL. Sorting of striatal and cortical interneurons regulated by semaphorin/neuropilin interactions. Science. 2001; 293:872–875. [PubMed: 11486090]

42. Frazer S, et al. Transcriptomic and anatomic parcellation of 5-HT3AR expressing cortical interneuron subtypes revealed by single-cell RNA sequencing. NatCommun. 2017; 8:14219.

43. Tanaka DH, Maekawa K, Yanagawa Y, Obata K, Murakami F. Multidirectional and multizonal tangential migration of GABAergic interneurons in the developing cerebral cortex. Development. 2006; 133:2167–2176. [PubMed: 16672340]

44. Yokota Y, et al. Radial glial dependent and independent dynamics of interneuronal migration in the developing cerebral cortex. PLoS One. 2007; 2:e794. [PubMed: 17726524]

45. Rakic P. Neuron-glia interactions during granule cell migration in developing cerebellar cortex. A Golgi and electronmicroscopic study in macacus rhesus. J Comp Neurol. 1971; 141:283–312. [PubMed: 4101340]

46. de Frutos CA, et al. Reallocation of Olfactory Cajal-Retzius Cells Shapes Neocortex Architecture. Neuron. 2016; 92:435–448. [PubMed: 27693257]

47. Flames N, et al. Delineation of multiple subpallial progenitor domains by the combinatorial expression of transcriptional codes. J Neurosci. 2007; 27:9682–9695. [PubMed: 17804629]

48. Silberberg SN, et al. Subpallial Enhancer Transgenic Lines: a Data and Tool Resource to Study Transcriptional Regulation of GABAergic Cell Fate. Neuron. 2016; 92:59–74. [PubMed: 27710791]

49. De Marco Garcia NV, Karayannis T, Fishell G. Neuronal activity is required for the development of specific cortical interneuron subtypes. Nature. 2011; 472:351–355. [PubMed: 21460837]

50. Mi D, et al. Early emergence of cortical interneuron diversity in the mouse embryo. Science. 2018; doi: 10.1126/science.aar6821

51. Madisen L, et al. A robust and high-throughput Cre reporting and characterization system for the whole mouse brain. Nat Neurosci. 2010; 13:133–140. [PubMed: 20023653]

52. Taniguchi H, et al. A resource of Cre driver lines for genetic targeting of GABAergic neurons in cerebral cortex. Neuron. 2011; 71:995–1013. [PubMed: 21943598]

53. Batista-Brito R, Close J, Machold R, Fishell G. The distinct temporal origins of olfactory bulb interneuron subtypes. J Neurosci. 2008; 28:3966–3975. [PubMed: 18400896]

54. Sylwestrak EL, Ghosh A. Elfn1 regulates target-specific release probability at CA1-interneuron synapses. Science. 2012; 338:536–540. [PubMed: 23042292]

55. López-Bendito G, et al. Preferential origin and layer destination of GAD65-GFP cortical interneurons. Cereb Cortex. 2004; 14:1122–1133. [PubMed: 15115742]

56. Yu WM, et al. A Gata3-Mafb transcriptional network directs post-synaptic differentiation in synapses specialized for hearing. Elife. 2013; 2:e01341. [PubMed: 24327562]

57. Ng D, et al. Neto1 is a novel CUB-domain NMDA receptor-interacting protein required for synaptic plasticity and learning. PLoS Biol. 2009; 7:e41. [PubMed: 19243221]

58. Sousa VH, Miyoshi G, Hjerling-Leffler J, Karayannis T, Fishell G. Characterization of Nkx6-2-derived neocortical interneuron lineages. Cereb Cortex. 2009; 19(Suppl 1):i1–10. [PubMed: 19363146]

59. Vong L, et al. Leptin action on GABAergic neurons prevents obesity and reduces inhibitory tone to POMC neurons. Neuron. 2011; 71:142–154. [PubMed: 21745644]

60. Pla R, Borrell V, Flames N, Marín O. Layer acquisition by cortical GABAergic interneurons is independent of Reelin signaling. J Neurosci. 2006; 26:6924–6934. [PubMed: 16807322]

61. Englund C, et al. Pax6, Tbr2, and Tbr1 are expressed sequentially by radial glia, intermediate progenitor cells, and postmitotic neurons in developing neocortex. J Neurosci. 2005; 25:247–251. [PubMed: 15634788]

62. Bentley M, Decker H, Luisi J, Banker G. A novel assay reveals preferential binding between Rabs, kinesins, and specific endosomal subpopulations. J Cell Biol. 2015; 208:273–281. [PubMed: 25624392]

63. Tashiro A, Sandler VM, Toni N, Zhao C, Gage FH. NMDA-receptor-mediated, cell-specific integration of new neurons in adult dentate gyrus. Nature. 2006; 442:929–933. [PubMed: 16906136]

64. Pakan JM, et al. Behavioral-state modulation of inhibition is context-dependent and cell type specific in mouse visual cortex. Elife. 2016; 5

65. Williams SR, Mitchell SJ. Direct measurement of somatic voltage clamp errors in central neurons. Nat Neurosci. 2008; 11:790–798. [PubMed: 18552844]

66. Kaifosh P, Zaremba JD, Danielson NB, Losonczy A. SIMA: Python software for analysis of dynamic fluorescence imaging data. Front Neuroinform. 2014; 8:80. [PubMed: 25295002]

67. Keemink SW, et al. FISSA: A neuropil decontamination toolbox for calcium imaging signals. Sci Rep. 2018; 8:3493. [PubMed: 29472547]
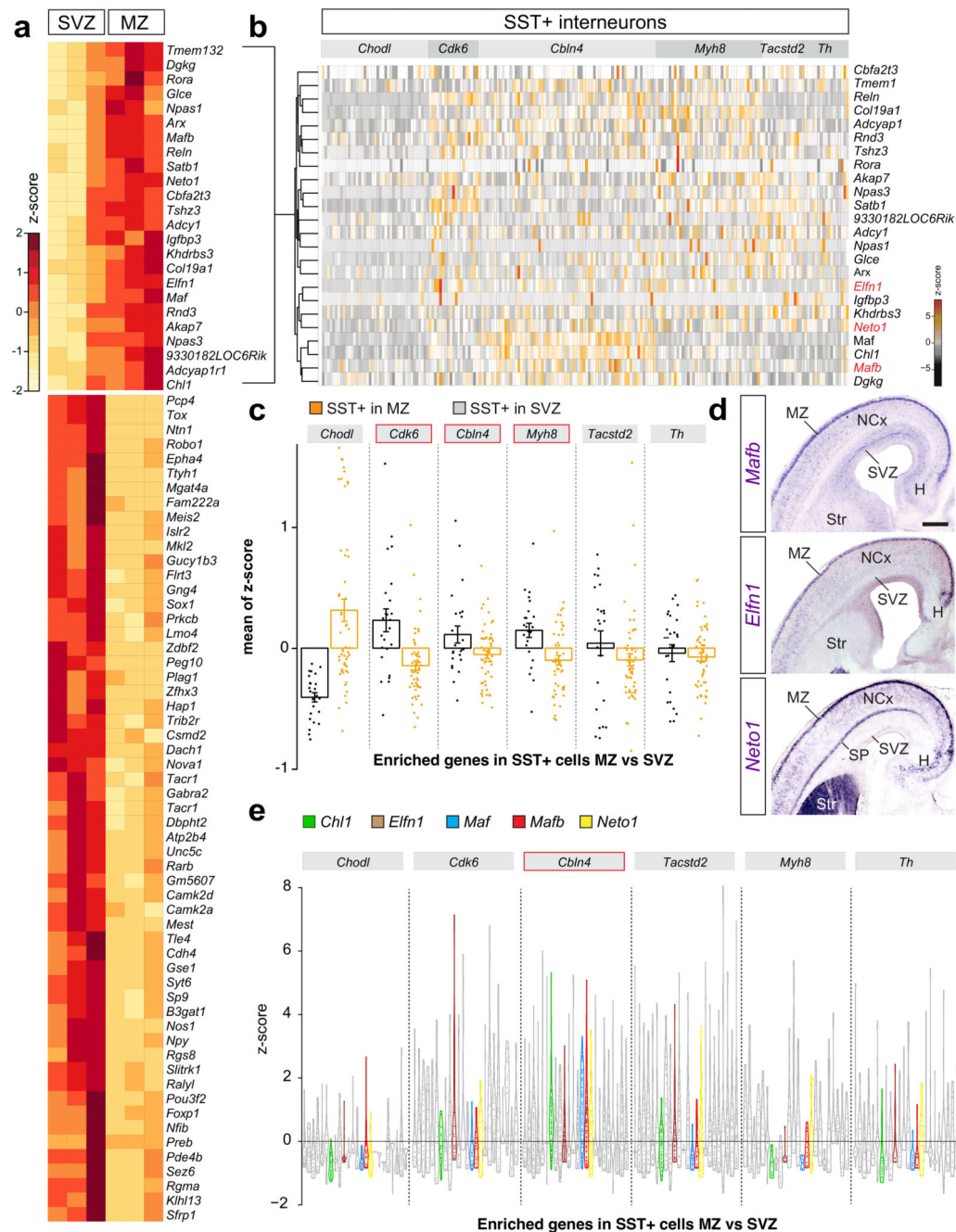
Figure 1. Different interneurons exhibit migratory route choice biases.
a–c, Coronal sections through the neocortex (NCx) showing immunohistochemistry for GFP in $Vgat^{Cre}$;RCE embryos at various stages, repeated with similar results in 3 animals. **d**, Bar graphs represent mean ± s. e. m for fraction of interneurons in the MZ ($n = 3$ animals per stage). **e,f,h,i**, Coronal sections through the E15.5 cortex of $Nkx2-1^{Cre}$;RCE (e) and $Gad65$-Gfp (f), Sst^{Cre};Ai9 (h), and $Dlx1/2^{CreER}$;Ai9, repeated with similar results in 3 animals (i) showing distribution of different groups of GABAergic interneurons. **g**, Cumulative frequency of fraction of interneurons in the marginal zone (MZ) for each genotype at all stages examined ($n = 12$ sections per animal, 3 animals per genotype and stage). **j**, Bar graphs represent mean ± s. e. m for fraction of interneurons in the MZ for each genotype at all stages examined ($n = 3$ animals per genotype and stage). Two-way ANOVA, post-hoc Tukey HSD, ***$p < 0.001$. H, Hippocampus; LGE, lateral ganglionic eminence; SVZ, subventricular zone. Scale bars equal 200 μm.

Figure 2. Different classes of SST+ interneurons migrate through distinct routes.
a, Heatmap representing relative levels (z-scores) of genes differentially expressed in SST+ cells migrating through the marginal zone (MZ) or the subventricular zone (SVZ) at E17.5, with FDR set at < 5% using the Benjamini-Hochberg method (*n* = 3 litters of embryos). **b**, Heatmap representing relative levels (z-scores) of MZ-enriched genes (from a) in different classes of SST+ interneurons from the adult visual cortex (data from Ref. 8). **c**, Bar graph represent mean ± s. e. m. z-scores for all MZ- (b) and SVZ-enriched genes (Supplementary Fig. 5) expressed in SST+ interneurons (*n* = 41 cells for *Chodl*, 19 for *Cdk6*, 68 for *Cbln4*,

14 for *Tascst2d*, 41 for *Myh8*, 33 for *Th*). The red boxes indicate molecularly distinct classes of SST+ interneurons with positive mean z-scores in MZ-enriched genes. **d**, Coronal sections through the E17.5 telencephalon illustrating mRNA expression of *Mafb*, *Elfn1* and *Neto1*, repeated in 2 animals with similar results. **e**, Violin plot showing individual cell (dot) of z-scores for individual MZ-enriched genes at E17.5. Five genes are highlighted based on expression ($n = 41$ cells for *Chodl*, 19 for *Cdk6*, 68 for *Cbln4*, 14 for *Tascst2d*, 41 for *Myh8*, 33 for *Th*). Five genes are highlighted based on expression. Three genes show positive mean z-scores uniquely in SST+/Cbln4+ cells (putative Martinotti cells) and negative or zero mean z-scores in all other populations of SST+ interneurons. H, hippocampus; NCx, neocortex; SP, subplate; Str, striatum. Scale bar equals 250 μm.
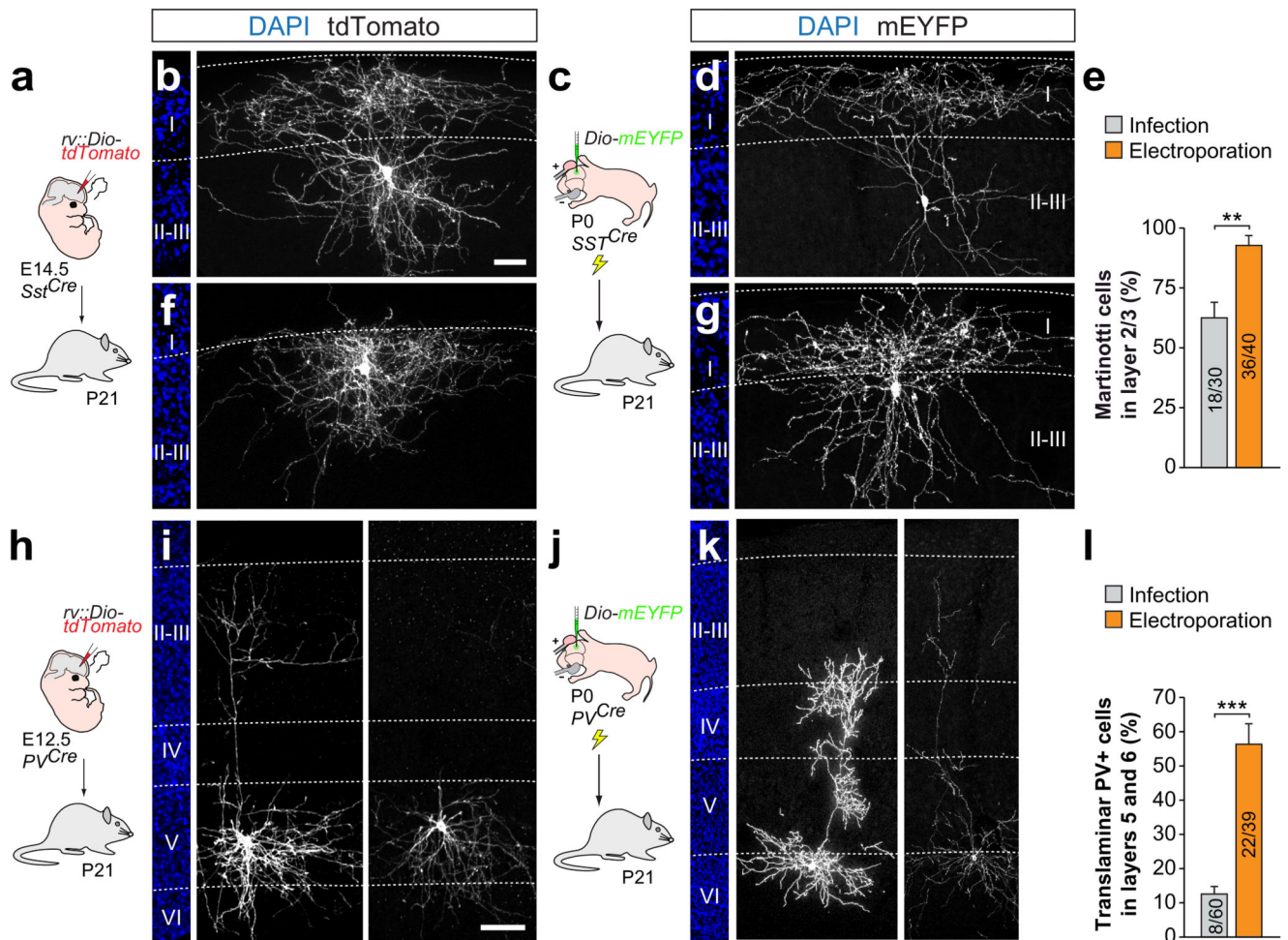
Figure 3. Martinotti cells and PV+ translaminar interneurons preferentially migrate through the MZ.

a,h, Schematic of experimental design for the labeling of interneuron progenitor cells using conditional retroviruses in Cre-expressing embryos. **c,j**, Schematic of experimental design for the labeling of interneurons migrating through the marginal zone (MZ) using pial surface electroporation of conditional reporter plasmids in Cre-expressing embryos. **b,d,f,g**, Representative images of SST+ interneurons at P21 obtained through viral labeling at E14.5, repeated with similar results in 30 cells from 5 animals (b,f) or pial surface electroporation at P0, repeated with similar results in 40 cells from 10 animals (d,g). **e**, Quantification of the proportion of Martinotti cells found in viral labeling and pial surface electroporation experiments ($n = 30$ and 40 cells from 5 and 10 animals for viral injections and electroporation, respectively). Error bars represent binomial proportion confidence interval. Two-tailed Fisher's exact test, **$p = 0.004$. **g,i**, Representative images of translaminar PV+ interneurons (g, left panel; i, both panels) and intralaminar PV+ interneurons (g, right panel) at P21 obtained through viral labeling at E12.5, repeated with similar results in 60 cells from 7 animals (g) or pial surface electroporation at P0, repeated with similar results in 39 cells from 8 animals (i). **l**, Quantification of the proportion of translaminar PV+ interneurons found in viral labeling and pial surface electroporation experiments ($n = 60$ and 39 cells

from 7 and 8 animals for viral injections and electroporation, respectively). Fisher's exact test, ***$p = 1.108e-05$. Scale bar equals 50 μm.
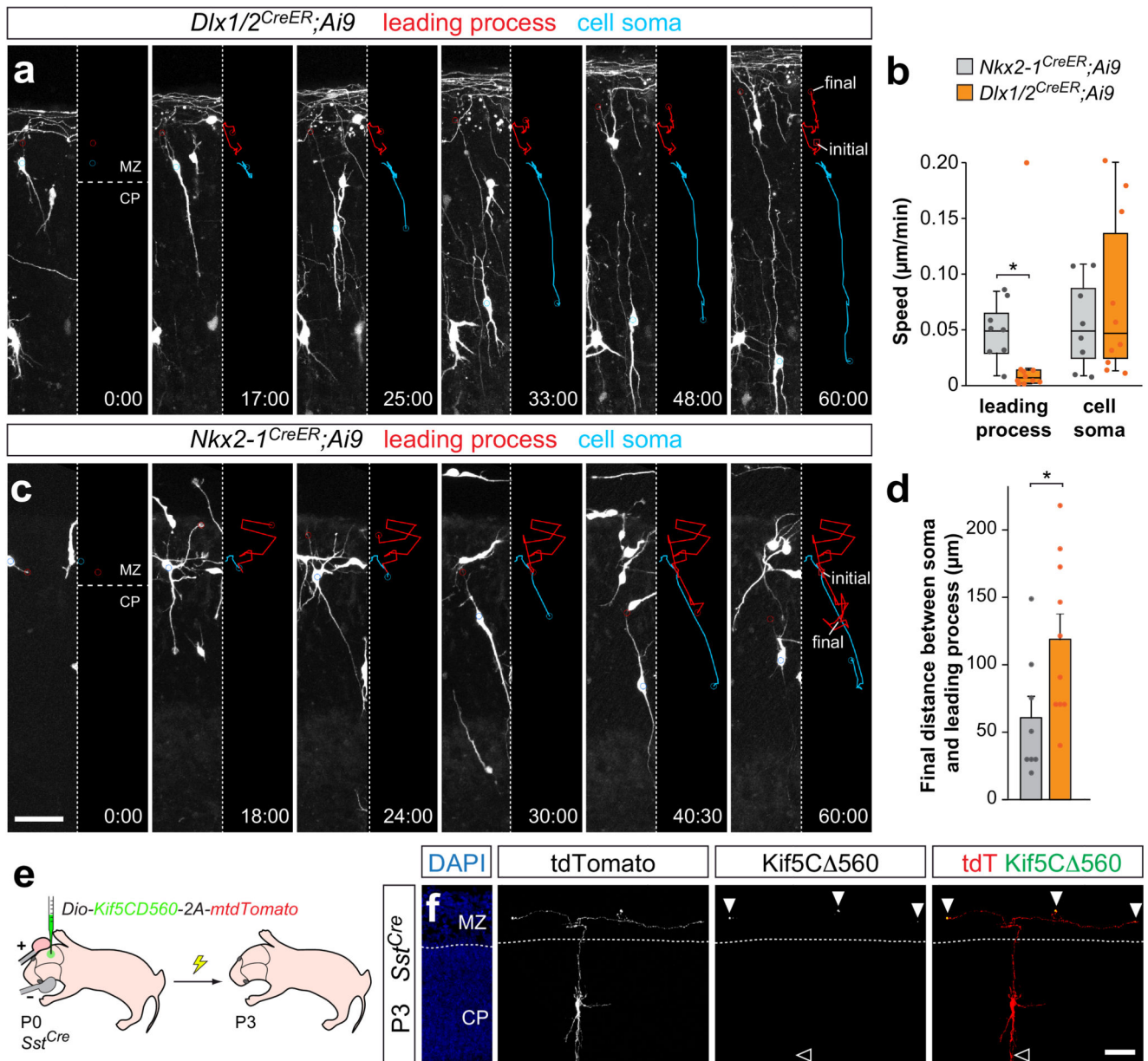
Figure 4. Martinotti cells leave their nascent axon in the MZ while migrating into the cortical plate.

a,c, Time-lapse images of migrating interneurons in coronal slices through the cortex of P0 *Dlx1/2^CreER^;Ai9* (a) and *Nkx2-1^CreER^;Ai9* (c) over a period of 60 h. Time-lapse experiments were repeated with similar results in 11 and 8 cells from 8 and 5 animals, respectively. For each time, track lines represent the trajectory of the cell soma (blue) and the tip of the neural process (red) closest to the marginal zone (MZ). Dotted lines represent the boundary between the MZ and cortical plate (CP). **b**, Box plots represent median, 1st and 3rd quartile, and 1.5 IQR of the speed of each cell soma or process tip $n = 11$ and 8 cells from 8 for *Dlx1/2^CreER^;Ai9* and 5 *Nkx2-1^CreER^;Ai9* mice, respectively. Two-tailed Mann Whitney U test with Bonferroni correction, *$p = 0.02$. **d**, Bar graphs represent mean ± s. e. m. for

distance between the cell soma and the tip of the trailing process after 60 h ($n = 11$ and 8 cells from 8 for *Dlx1/2^{CreER};Ai9* and 5 *Nkx2-1^{CreER};Ai9* mice, respectively). Two-tailed Student *t*-test, $*p = 0.03$. **e**, Schematic of experimental design for the labeling of nascent axons in prospective Martinotti cells via pial surface electroporation at P0. **f**, Representative image of a prospective Martinotti cell at P3, repeated in 14 cells from 5 animals, of which 11 cells showed similar results. Arrowheads point to Kif5C 560 expression in the nascent axon; the open arrowhead indicates lack of Kif5C 560 expression in the leading process. Scale bars equal 100 μm (a,c) and 50 μm (f).
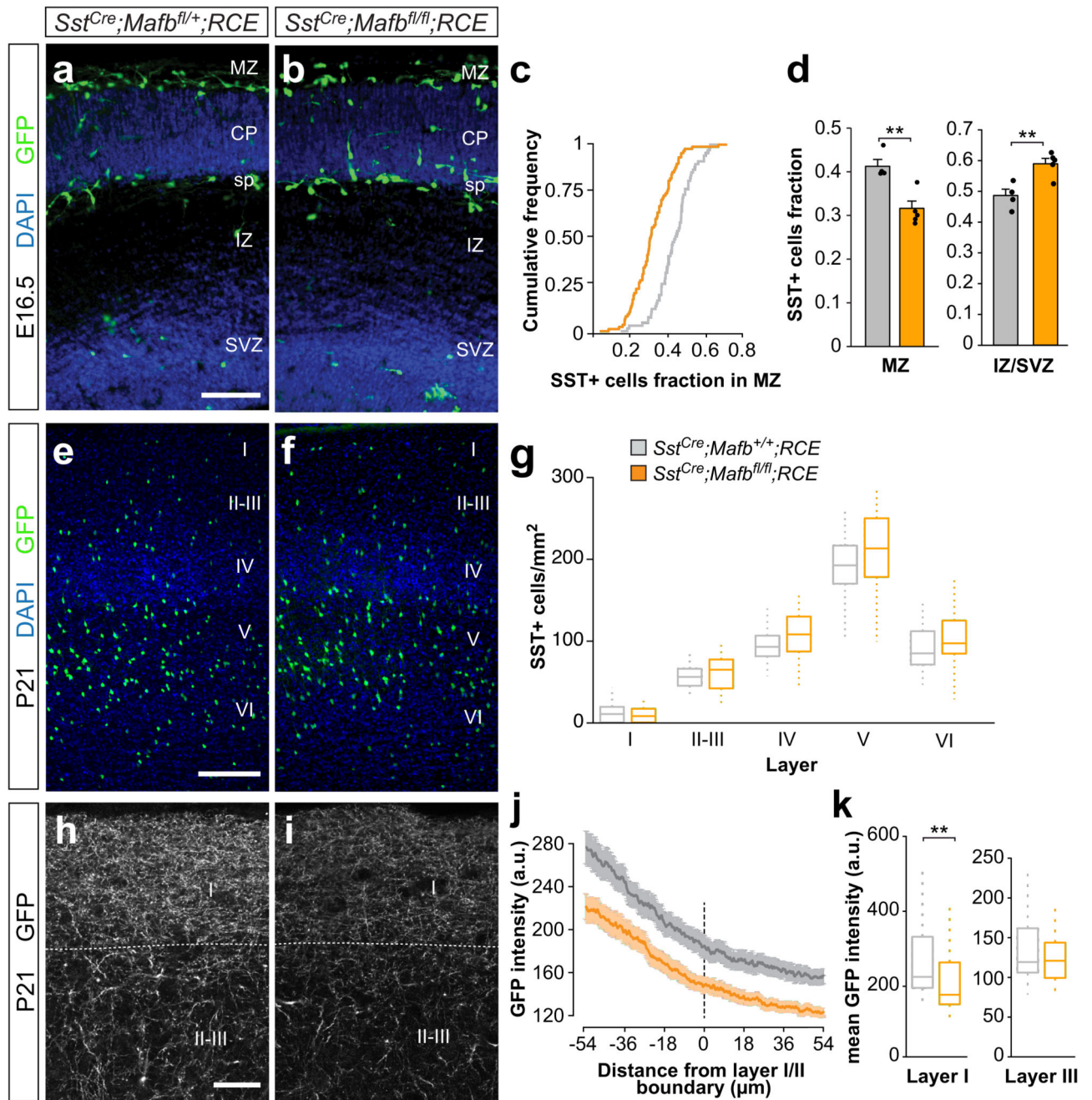
Figure 5. Abnormal migration of SST+ interneurons in conditional *Mafb* mutant mice.
a,b,e,f, Coronal sections through the cortex of E16.5, repeated with similar results in 4 and 5 mice per genotype (a,b) and P21, repeated with similar results in 3 mice per genotype, showing the distribution of SST+ (GFP+) interneurons in *Sst^Cre; Mafb^{fl/+};RCE* (a,e) and *Sst^Cre;Mafb^{fl/fl};RCE* (b,f) mice. **c,** Cumulative frequency plot of the fraction of cells in the marginal zone (MZ) for each genotype. **d,** Quantification of the fraction of SST+ cells migrating through the MZ ($n = 4$ control and 5 mutant mice). Two-tailed Student t-test, **$p = 0.004$ for MZ, **$p = 0.007794$ for SVZ. **g,** Boxplots represent median, 1st and 3rd quartile,

and 1.5 IQR of laminar distribution of SST+ (GFP+) cells in the neocortex ($n = 12$ sections per animal, 3 mice per genotype). Two-way ANOVA, $p = 0.90$. **h,i**, Coronal sections through the cortex of P21 $Sst^{Cre};Mafb^{fl/+};RCE$ (h) and $Sst^{Cre};Mafb^{fl/fl};RCE$ (i) mice illustrating the distribution of SST+ (GFP+) axons in layers 1 and 2/3 of the somatosensory cortex. **j**, Line charts representing relative GFP intensity at various distances from the layer I-layer II boundary. Dark lines and light shadings represent means and s.e.m. for both genotypes. $n = 10$ sections per animal, 5 mice per genotype. **k**, Boxplots represent median, 1st and 3rd quartile, and 1.5 IQR of mean GFP intensity in layers I (right) and III (left) of the neocortex; $n = 10$ sections per animal, 4 mice per group; two-way ANOVA, **$p = 0.004$. CP, cortical plate; IZ, intermediate zone; sp, subplate; SVZ, subventricular zone. Histograms represent mean ± s. e. m. Scale bars equal 100 μm (a,b,e,f) and 20 μm (h,i).
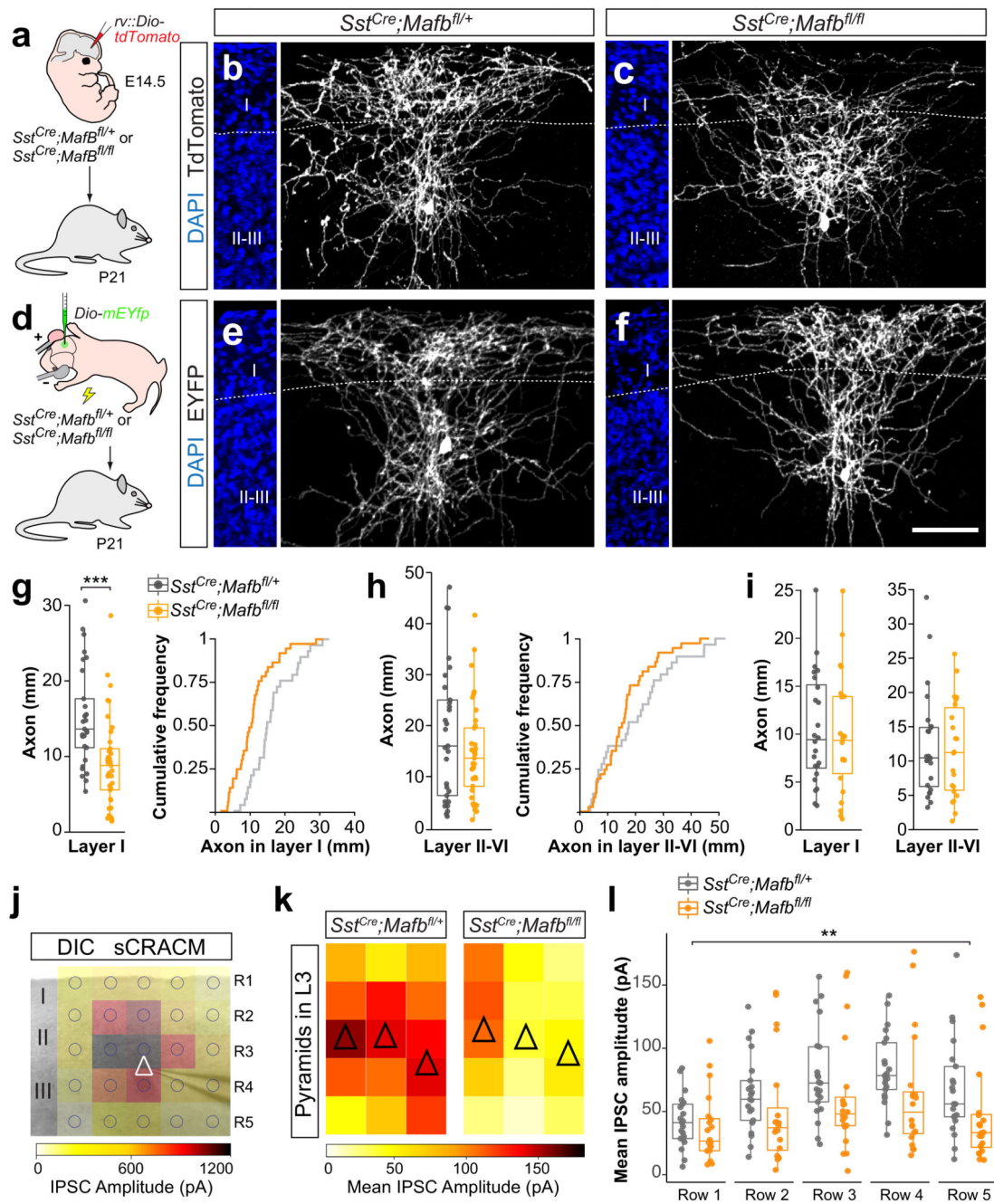
Figure 6. Abnormal development of Martinotti cell layer I axons in conditional *Mafb* mutant mice.

a, Schematic of experimental design for the labeling of interneuron progenitor cells using conditional retroviruses in Cre-expressing embryos. **b,c**, Coronal sections through the neocortex of P21 showing the morphology of Martinotti cells labeled through retroviral infection in *Sst^Cre^;Mafb^fl/+^* (b) and *Sst^Cre^;Mafb^fl/fl^* (c), repeated with similar result for *n* = 29 and 37 cells from 8 and 10 mice, respectively. **d**, Schematic of experimental design for the labeling of interneurons migrating through the marginal zone (MZ) using pial surface

electroporation of conditional reporter plasmids. **e,f**, Coronal sections through the neocortex of P21 showing the morphology of Martinotti cells labeled by pial electroporation in $Sst^{Cre};Mafb^{fl/+}$ (e) and $Sst^{Cre};Mafb^{fl/fl}$ (f), repeated with similar result for $n = 36$ and 32 Martinotti cells from 9 and 8 mice, respectively. **g,h**, Boxplots represent median, 1st and 3rd quartile, and 1.5 IQR of length of Martinotti cell axons labeled by retroviral infection in layer 1 (g) and layers 2-6 (h) at P21 ($n = 29$ and 37 Martinotti cells from 8 and 10 mice in control and mutant respectively). Two-tailed Student t-test with Bonferroni correction, ***$p = 0.0005$. Cumulative frequency plots for the length of Martinotti cell axons in layer 1 (g) and layers 2-6 (h) are shown next to the corresponding histograms. **i**, Boxplots represent median, 1st and 3rd quartile, and 1.5 IQR of length of Martinotti cell axons labeled by pial surface electroporation in layer 1 and layers 2-6 at P21 ($n = 36$ and 32 Martinotti cells from 9 control and 8 mutant mice, respectively). Two-tailed Student t-test with Bonferroni correction, $p = 0.681$ and $p = 0.911$, respectively. **j**, Schematic of experimental design for the subcellular ChR2-assisted circuit mapping (sCRACM) of SST+ interneuron outputs. Each circle depicts the target of a 70 μm^2 laser spot used to evoke inhibitory input onto a single recorded pyramidal cell, whose position is indicated by a white triangle. IPSC amplitude from each inhibitory spot is plotted as a heatmap in the overlaying image. R1-R5, rows 1 to 5. **k**, Representative laminar profiles of mean IPSCs recorded in layer 3 pyramidal cells from control and mutant mice. For these profiles, heatmaps were collapsed into one dimension by averaging evoked IPSC amplitude at each spot per row. The position of the recorded cells is indicated by a triangle. **l**, Boxplots represent median, 1st and 3rd quartile, and 1.5 IQR of IPSCs for each input row ($n = 21$ cells from 10 $Sst^{Cre};Mafb^{fl/+}$ mice and 19 cells from 11 $Sst^{Cre};Mafb^{fl/fl}$ mice). Two factorial ANOVA mean IPSC versus Genotype-Row, **$p = 0.004$.
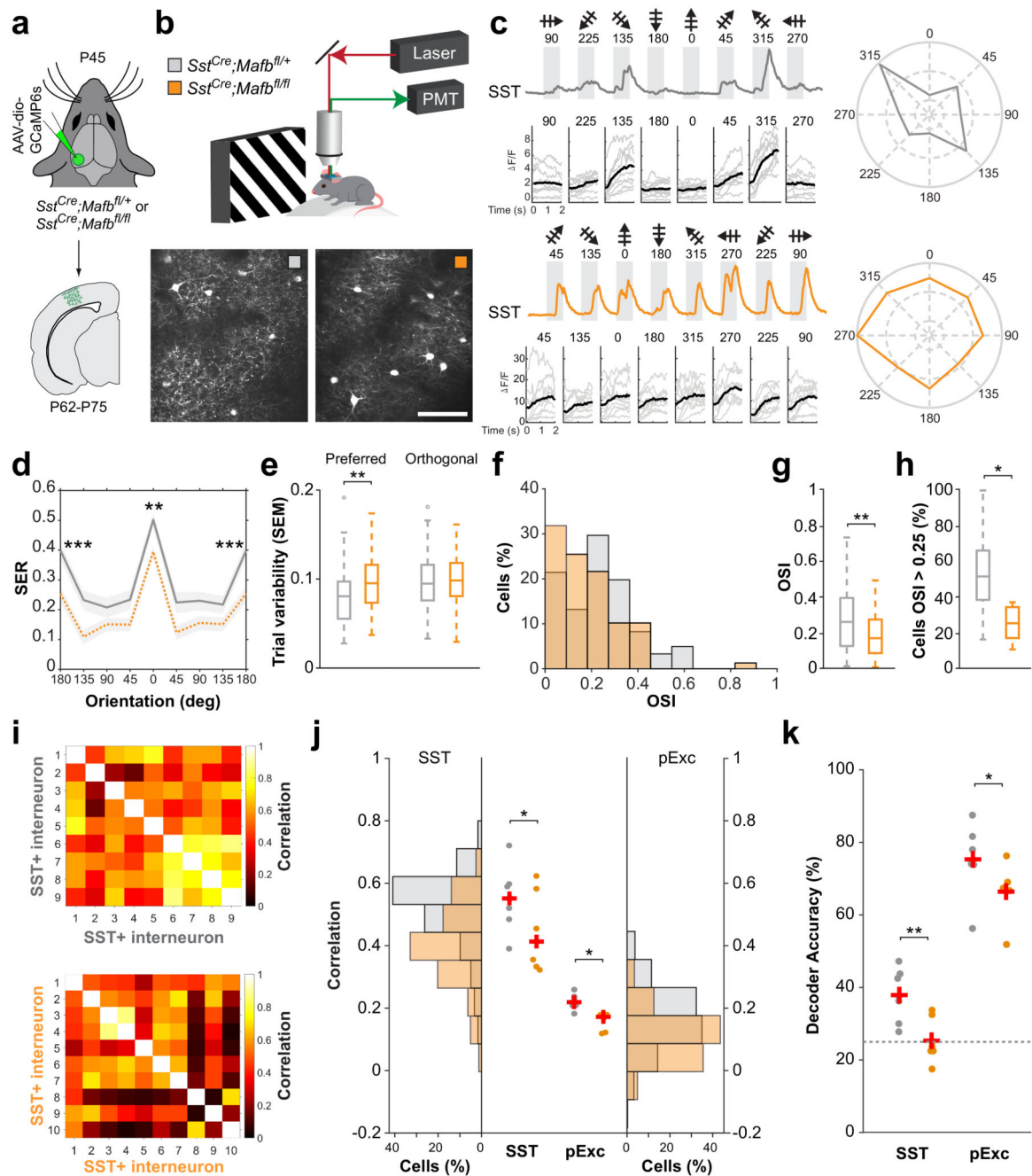
Figure 7. Impaired visual responses of SST+ interneurons in *Mafb* mutant mice.
a, Schematic of experimental design for the expression of GCaMP6s in SST+ interneurons using conditional AAV plasmids in Cre-expressing mice. **b**, Experimental set-up for two-photon calcium imaging in V1 of awake head-fixed mice and representative two-photon images of layer 2/3 SST+ interneurons labeled with GCaMP6s in $Sst^{Cre};Mafb^{fl/+}$ and $Sst^{Cre};Mafb^{fl/fl}$ mice. **c**, Calcium transients (F/F$_0$) of representative SST+ interneurons imaged during the presentation of 8 oriented drifting gratings (0 to 315°; arrows and numbers indicate the angle of drift direction). For each genotype, the upper trace shows a

single trial with grey regions indicating the periods of visual stimulation. The lower traces show the responses for all trials (grey) and the average response across trials (black). The orientation tuning polar plot is also shown for each neuron. **d**, Average tuning curve for all SST+ interneurons in $Sst^{Cre};Mafb^{fl/+}$ and $Sst^{Cre};Mafb^{fl/fl}$ mice, calculated from the average stimulus evoked response (SER) for each of the 8 directions of drifting gratings and normalized to the preferred direction. Light grey shading indicates SEM ($n = 61$ neurons from 7 $Sst^{Cre};Mafb^{fl/+}$ mice and 79 neurons from 7 $Sst^{Cre};Mafb^{fl/fl}$ mice). Kruskal-Wallis test, ***$p = 0.001$, **$p = 0.005$, orthogonal orientations $p = 0.063$. **e**, Boxplots represent median, 1st and 3rd quartile, and 1.5 IQR of trial-by-trial variability using the average standard error of the mean (SEM) of the stimulus-evoked responses (SER) across trials, for both the preferred orientation, **$p = 0.005$ and for the orientation orthogonal to the preferred $p = 0.314$ ($n = 61$ neurons from 7 $Sst^{Cre};Mafb^{fl/+}$ mice and 79 neurons from 7 $Sst^{Cre};Mafb^{fl/fl}$ mice). Kruskal-Wallis test. **f**, Quantification of the distribution of orientation selectivity indices (OSI) of SST+ interneurons for each genotype. **g**, Boxplots represent median, 1st and 3rd quartile, and 1.5 IQR of OSI for all SST+ interneurons for each genotype ($n = 61$ neurons in $Sst^{Cre};Mafb^{fl/+}$ mice and 79 neurons in $Sst^{Cre};Mafb^{fl/fl}$ mice). Kruskal-Wallis test, **$p=0.009$. **h**, Boxplots represent median, 1st and 3rd quartile, and 1.5 IQR for percentage of orientation selective neurons (OSI > 0.25) for each field of view per genotype ($n = 7$ fields of view for each genotype). Kruskal-Wallis test, *$p = 0.015$. **i**, Pairwise correlation (Pearson correlation coefficient) matrices for all SST+ interneurons in one representative field of view for each genotype ($n = 9$ neurons in $Sst^{Cre};Mafb^{fl/+}$ mice and 10 neurons in $Sst^{Cre};Mafb^{fl/fl}$ mice). **j**, The central panel shows the average of all pairwise correlations for each field of view, between SST+ interneurons (left; $p = 0.035$) and between putative excitatory neurons (pExc) (right; $p = 0.016$), for each genotype. Red crosses indicate the average across all fields of view ($n = 7$ fields of view for each genotype for SST + interneurons and 6 fields of view for each genotype for pExc neurons). Kruskal-Wallis test. The side panels show quantification of the distribution of pairwise correlations between SST+ interneurons (left) ($n = 61$ neurons from 7 $Sst^{Cre};Mafb^{fl/+}$ mice and 79 neurons from 7 $Sst^{Cre};Mafb^{fl/fl}$ mice) and pExc neurons (right) ($n = 1321$ neurons from 7 $Sst^{Cre};Mafb^{fl/+}$ mice and 1424 neurons from 7 $Sst^{Cre};Mafb^{fl/fl}$ mice). **k**, Classification accuracy of a template-matching decoder trained on the activity of SST+ interneurons or pExc neurons to decode grating identity. Red crosses indicate the average across all fields of view. Dashed line indicates chance level of decoding accuracy ($n = 7$ fields of view for each genotype for SST+ interneurons, **$p = 0.008$ and 6 fields of view for each genotype for pExc neurons, $p = 0.032$). Kruskal-Wallis test. Scale bar equals 100 μm. All boxplots represent median, 1st and 3rd quartile, and 1.5 IQR.